Effects of build orientation on 3D printed Co-Cr-Mo: Surface topography and L929 fibroblast cellular response

Alfred T. Sidambe[1,2]*

1. Bioengineering & Health Technologies Group, School of Clinical Dentistry, University of Sheffield, 19 Claremont Crescent, Sheffield, S10 2TA UK; E-Mail: a.t.sidambe@gmail.com

2. Mechanical, Materials and Aerospace Engineering, School of Engineering, University of Liverpool, Brownlow Hill, Liverpool, L69 3GH; E-Mail: a.sidambe@liverpool.ac.uk

* Author to whom correspondence should be addressed; E-Mail: a.t.sidambe@gmail.com;

Abstract

Selective Laser Melting (SLM) is increasingly being used for the fabrication of cobalt chromium customised medical devices. The purpose of this study was to determine the effect of surface topographies from SLM parts on the in-vitro biological responses of mouse fibroblasts (L929). Fibroblast cells were cultured for 3 days on SLM and on conventionally cast Co-Cr-Mo surfaces and their proliferation, morphology, viability and cytotoxicity investigated. SLM processing parameters were used to manufacture discs with different microlevel surface topographies. Our analysis showed that the SLM implants met basic biocompatibility requirement on all surfaces. The effect of the SLM processing parameters was characterised by an improvement in cell viability with increasing surface roughness. The number of viable cells on all the SLM Co-Cr-Mo either equaled or was higher than those on the reference cast sample. A statistically significant difference ($p<0.05$) was found between the cell viability on two SLM specimens (R_a=29.25 and 20.62μm) and reference cast (R_a=4.32μm). In comparison to a polymeric negative control, the absorbance measurement on Co-Cr-Mo surfaces was in the range of 60 to 80% of the control and the cytotoxicity was comparable to the cast sample. The surface roughness amplitude parameters were found to discriminate cell viability and cytotoxicity better, confirming that fibroblast cell growth on SLM surfaces was more influenced by the amplitude rather than by the organisation or morphology of the surface. It is concluded that SLM processing significantly affects surface topography which in turn influences the L929 fibroblast cellular response.

Keywords: Selective Laser Melting, Cobalt Chrome, CoCr, Co-Cr-Mo, Biocompatibility, Powder Metallurgy, Additive Manufacturing, 3-D Printing, Dental Implants, Cytotoxicity.

Graphical Abstract

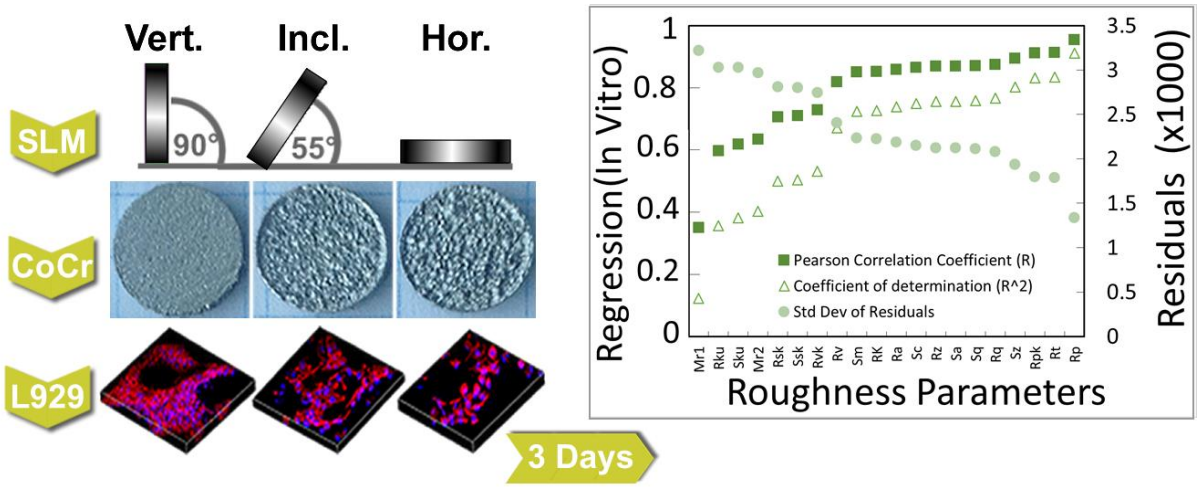

1 Introduction

Cobalt Chromium alloy (Co28Cr6Mo or Co-Cr-Mo) alloys are preferred for use in biomedical applications such as dental and orthopaedic implants because they possess excellent mechanical properties and have good biocompatibility [1,2]. However, Co-Cr-Mo production is hampered by the time consuming, costly processes in traditional manufacturing and poor workability for complex shape production [3,4]. As a result, developments over the last two decades have seen powder based additive manufacturing (AM) processes such as selective laser melting (SLM) emerge as alternative techniques that can minimise the cost of production, particularly for complex shapes because they enable production of near net shape components [5,6]. SLM, often also referred to using the terms direct metal laser sintering (DMLS) or selective laser sintering (SLS), is preferred for fabricating Co-Cr-Mo alloys in the medical sector because it offers the ability to make patient specific, complex, cellular and functional mesh arrays implants or bone substitutes [5]. Selective laser melting is a powder-bed additive manufacturing process in which the material is added one cross-sectional layer at a time to create a three-dimensional object from a CAD model [7-10].

The nature of the SLM process which involves laser melting of powder one layer after another at specific thicknesses carries with it some opportunities such as using the layer thickness, laser power, part orientation, laser diameter, scanning speed, hatch strategy and hatching distance parameters to customise surfaces, some of which are used in biomedicine to promote cell growth or osseointegration [11-15]. These parameters determine the energy supplied by the laser beam to a volumetric unit of powder material, defined as energy density [12,16]. When optimised, the above mentioned SLM parameters are able to minimise part defects such as pores, cracks, distortion, warping and residual stress. Eliminating such defects

improves the properties of the finished parts such as strength, hardness, microstructure, surface finish and biocompatibility [8,17] [18,19].

Medical devices fabricated using relatively new processes such as SLM have to demonstrate biomedical and biomechanical safety as regulated by bodies such as the US Food and Drug Administration, ASTM and ISO [20] [21,22] [23] [24,12]. Carrying out clinical studies of SLM Co-Cr-Mo devices is the methodology which has seen an increase in the acceptance of this technology by the worldwide biomedical as well as dental community [19]. In the ongoing research into the biocompatibility of SLM Co-Cr-Mo researchers have found that the SLM process can influence the biocompatibility of the devices fabricated. The Co-Cr-Mo medical devices processed using the SLM process are expected to have better alloy homogeneity as a result of the fine metallic powders contributing to a fine-grain structure. The effect of such a microstructure on the biocompatibility properties of SLM Co-Cr-Mo has been investigated and found to decrease the corrosion and metal release susceptibility of the SLM Co-Cr-Mo alloy in comparison to the cast counterpart [3]. Additionally, in biomedical applications, alterations in the elemental composition can influence the cytotoxicity of an alloy such Co-Cr-Mo [25]. The unique textures formed in the pattern of the melting pools of the SLM Co-Cr-Mo alloy have been shown to have less ion release than cast as well as have good cell viability[18] [26] [27] [25]. Furthermore, the susceptibility for corrosion and metal ion release in SLM Co-Cr-Mo has been shown to increase with an increased number (area) of laser melt pool boundaries [3,28], indicating that the process parameters within the SLM process can be used to influence the biocompatibility properties. However the research being carried out so far has not specifically looked at the SLM processing parameters as an enabling tool for customising the solid (non-lattice) structure surface topography and how this affects the in-vitro biocompatibility of the Co-Cr-Mo.

In this regard, this study was carried out to determine the effect of processing parameters on the Co-Cr-Mo alloy using different parameters based on the volumetric laser energy density and part orientation in the build chamber. The emphasis was to use the SLM parameters to manufacture discs with different microlevel surface topographies. The use of a rough surfaces to promote biocompatibility properties such as osseointegration is well established and engineering of the surface topographies is carried out by various means of grit blasting followed by a surface etching or coating procedure [29]. SLM is a process which can produce rough topographies in a single processing routine. Therefore, studies were carried out to find out whether the SLM processing affects the in-vitro biocompatibility of the Co-Cr-Mo alloy because understanding the effect of surface topography on cellular response is crucial, particularly for tissue engineering given that many natural tissues have topographical features which affect cell behaviour by altering protein adsorption [30] [31].

2 Materials and Methods

2.1 Selective Laser Melting of Co-Cr-Mo

A Renishaw SLM 125 system (Stone, UK) was used to melt gas atomised Co-Cr-Mo alloy (CoCr2LC) supplied by LPW Technology (Runcorn, UK). Two different volumetric laser energy densities (also referred to as 3-dimensional (3D) specific energy [32-34]) of 88 J/mm^3 (Co-Cr-Mo88) and 208 J/mm^3 (Co-Cr-Mo208) were used to fabricate SLM discs (10mm diameter x 2mm height). The volumetric laser energy density was derived from 3D specific energy input by combining laser power, laser scan speed, layer thickness, and hatch spacing [32,35-37]. The 3D formulation can be seen as Equation 1 below:

$$\varepsilon_{Density} = \frac{P_{Laser}}{v_{scan} . S_{hatch} . t_{layer}} \qquad Eqn\ 1$$

$\mathcal{E}_{Density}$ is the 3 dimensional input laser energy density, P_{laser} is the laser power, v_{scan} is the laser scan speed, s_{hatch} is the hatch spacing and t_{layer} is the layer thickness. The processing parameters were applied to parts orientated in the horizontal (0°), inclined (55°) and vertical (90°) planes in the SLM build chamber.

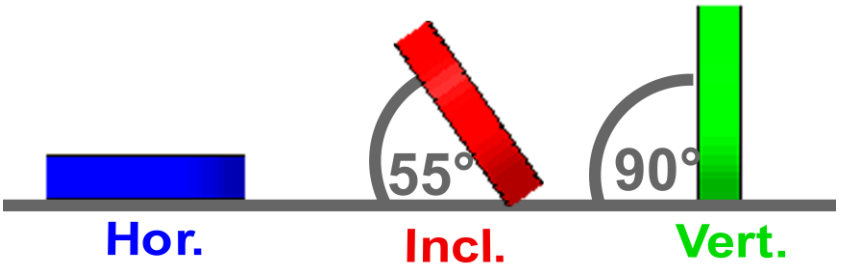

Fig 1: CAD illustrations of the orientations of the Co-Cr-Mo discs in the SLM system build chamber.

Fig 1 shows the CAD illustrations of the orientations of the Co-Cr-Mo discs in the horizontal (0°), inclined (55°) and vertical (90°) planes in the SLM system build chamber. The angles of orientation were calculated with reference to the horizontal axis (x-y Cartesian plane). At this juncture we would like to caution the reader that many authors within additive manufacturing refer to the build direction (vertical) as the 0° orientation and the build plate direction (horizontal) as the 90° orientation, and suggest that particular attention must be paid to the terminology used by different investigators.

2.2 Surface characteristics

	Parameter	Meaning	Ref
(A)	Ra (µm)	Average roughness	[38]
	Rq (µm)	Root mean square parameter average roughness	[38]
	Rp (µm)	The height of the highest peak in the roughness profile	[38]
	Rv (µm)	Maximum profile valley depth	[38]
	Rt (µm)	Amplitude range. The sum of R_p and R_v.	[38]
	Rz (µm)	Mean maximal amplitude of five highest peaks	[39]
	Rsk	Skewness of amplitude distribution function (ADF).	[39]
	Rku	Kurtosis - the spikiness of the profile	[39]
(B)	Mr1 (%)	The fraction of the surface which consists of small peaks	[40]
	Mr2(%)	The fraction of the surface that consists of deeper valleys	[40]
	Rvk(µm)	Reduced valley depths along (x,y) from bearing ratio curve	[39]
	Rpk (µm)	Reduced peak height along (x,y) from bearing ratio curve	[39]
	Rk(µm)	Peak to valley roughness along (x,y) from bearing ratio curve	[39]
(C)	Sa (µm)	Average roughness within a definition area (A)	[41]
	Sq (µm)	Root mean square roughness within a definition area (A)	[41]
	Sz (µm)	The peak to valley height within area (A)	[41]
	Ssk	Skewness of the 3-D surface texture	[41]
	Sku	Kurtosis of the 3-D surface texture	[41]
(D)	Sm (mm^3/mm^2)	The mean spacing between peaks	[42]
	Sc (mm^3/mm^2)	Core void volume	[42]

Table 1: Definitions of the surface roughness parameters that were analysed for correlation with cell growth. The classification of the parameters is as follows: (A) 2D amplitude, (B) 2D functional, (C) 3D amplitude and (D) 3D functional. [38,39,41,42].

After fabrication, the SLM discs were cleaned in order to remove loose metallic particles from the surfaces of the parts. Topographical characterisation of the surface profiles was then carried out before cell culture using the Contour GT 3D Optical Profiler (Bruker UK Ltd, Coventry, UK). The profiler was used in conjunction with the Vision32 and Vision64™ software. The Contour GT is based on the fundamental science of white light interferometry

and is designed to deliver high resolution images and surface measurements [43,38]. The surface topography is often defined only by an average roughness amplitude parameter (R_a), but in this study we measured a range of 2-dimensional (2D) and 3D amplitude, spatial, hybrid and functional parameters. The functional parameters were selected with the aim of investigating whether they affect the cell growth through adhesion and the frequency parameters such as Sm were measured in order to study the effect of the organisation of the topography on cell viability [44,45]. Table 1 shows the definitions of the surface roughness parameters that were analysed. The reader is also referred elsewhere for a comprehensive definition of the relevant parameters [39-42]. The local deviations of the surfaces, also widely referred to as the surface texture [45] were studied using the Inspect-F50 (FEI, Oregon,USA) and Philips XL 20 (Royal Philips Electronic, Eindhoven, The Netherlands) SEM's operated with an accelerating voltage of 20 kV also before cell culture. The SLM surfaces were compared to reference cast disc samples prepared according to the ISO 22674 type 5 Nickel and Beryllium free alloy [21].

2.3 Cell Culture

It is well known that the surface properties of biomaterials influence the adsorption of proteins from culture medium and therefore the methods below were considered to be suitable for biocompatibility testing [30]. The disc samples were initially sterilised by rinsing them in methylated industrial spirit (IMS, Fisher Scientific, Loughborough, UK), phosphate buffer saline (PBS, pH 7.4) from Sigma-Aldrich, Dorset, UK and in distilled water for a total of 15 minutes. Further sterilisation was carried out by steam autoclaving for 30 min at 120°C. Cell culture was carried out using the L929 fibroblast cells (ATCC, Rockville, MD, USA) at passage 32. The L929 fibroblast cell was selected because it is an established and robust cell line recommended according to ISO 10993-5 standards on *in vitro* cytotoxicity testing [46].

The L929 fibroblast cells were cultured in Dulbecco's Modified Eagle Medium nutrient mixture (DMEM, Fisher Scientific) supplemented with Non-essential amino acids (N.E.A.A) from Lonza, UK, Penicillin Streptomycin (PS), Lglutamin (Sigma-Aldrich), Hepes (Sigma-Aldrich) and 10% Fetal Calf Serum (FCS, Sigma-Adrich). Cells were placed into T75 cell culture flasks and incubated at 37°C and 5% CO_2/Air. $1x10^6$ cell were seeded per T75 flask. Medium was changed every 3 days until the cells were confluent. The cells were harvested and then seeded on the Co-Cr-Mo SLM discs as well as on the cast Co-Cr-Mo discs which were placed in 24-well cell culture plates. Cells on Co-Cr-Mo implant discs were cultured in the same nutrient mixture as described above and then incubated for 3 days. 0.25×10^6 L929 cells were seeded per Co-Cr-Mo disc.

2.3.1 Cell Morphology

The 3 day cell morphology and spread was analysed using SEM and fluorescent confocal microscopy. The Co-Cr-Mo and cast discs were moved onto new 24-well plates using sterile tweezers. In order to fix the cells, 3ml of 0.1M cacodylate buffer (buffer) was added to each well plate and left for 5 minutes. Attached cells were fixed with 3% glutaraldehyde in 0.1M cacodylate buffer (Sigma-Aldrich, UK) for 30 minutes at room temperature and then washed three times with buffer. A postfix treatment in 2% osmium tetroxide (Sigma-Aldrich, Dorset, UK) for 2 hours at room temperature was then carried out. After washing in buffer, the cells were then dehydrated through increasing concentrations of ethanol (70, 95, 100% Fisher Scientific). Dehydrated Co-Cr-Mo discs were then immersed in 50% hexamethyldisilazane/50% dried ethanol for one hour, then left in hexamethyldisilazane overnight. The discs were sputter-coated with gold for 30 seconds at a current of 35 mA, and

examined using the Inspect-F50 (FEI, Oregon,USA) and Philips XL 20 (Royal Philips Electronic, Eindhoven, The Netherlands) SEM's.

The 3 day cells were also prepared for morphological and genetic expression (ie cytoskeleton) analysis via confocal fluorescent microscopy. The cells were fixed, their actin filaments and nucleii stained and then images were taken. The media was removed and the cells were washed once with PBS after which the discs were moved to new 24-well plates. The cells were fixed with 3.7% formaldehyde solution for 20 minutes at room temperature. The cells were then washed 3 times with PBS twice for five minutes. After that, 0.1% (v/v) Triton X 100 solution was added then cells were incubated for 30 minutes at room temperature and then washed 3 times again with PBS. Phalloidin-TRITC (red) (Phalloidin, Fluorescein Isothiocyanate, Sigma-Aldrich) solution was added to the cells and incubated for 30 minutes at room temperature in the dark by covering the plate in aluminium foil. The cells were again washed three times with PBS. In order to label cell nuclei, a solution of Hoescht 33342 (Thermo Scientific, Altrincham, UK) was used and incubated for 15 minutes at room temperature in the dark. After washing again three times with PBS, the cells were ready for imaging. Images (512 x 512 pixel size) were obtained using a Zeiss LSM 510Meta upright confocal microscope (Carl Zeiss, Oberkochen, Germany) equipped with an Achroplan 40x/0.8W objective, using pixel dwell times of 25.6µs and 34.5µs. All image analysis was performed using the Zeiss LSM Image Browser and Zeiss ZEN lite software.

2.3.2 Cell Viability

The viability of the L929 cells cultured on SLM Co-Cr-Mo (n=12) and cast discs was carried out using fluorescent and calometric methods. The PrestoBlue® Cell Viability Reagent (Life Technologies, Paisley, UK) was used to detect metabolic activity. PrestoBlue®

is a ready to use cell permeable resazurin-based solution that functions as a cell viability indicator by using the reducing power of living cells to quantitatively measure the proliferation of cells [47] . The discs containing cultured cells were washed with PBS and placed into new well plates using sterile tweezers and the assay was performed in the dark because PrestoBlue is light sensitive. A 1:10 dilution of PrestoBlue® in DMEM media was prepared and 2ml of PrestoBlue® was added to each well plate containing a Co-Cr-Mo disc specimen. 2ml was added to empty wells as a control measure and then the 24-well plate was placed in the incubator. After 30 minutes and 60 minutes, 200µl of PrestoBlue® was removed from each well and transfered into wells of a 96-well plate in triplicate order. The 96 well plate was then placed in a Tecan plate reader (Tecan, Switzerland) and the fluorescence was read at excitation wavelength of 530nm with 590nm emission wavelength using the Magellan™ data analysis software.

2.3.3 Cytotoxicity

The L929 mouse fibroblasts (n=6) were counted using the CytoTox 96® non-radioactive cytotoxicity assay (Promega UK, Southampton, UK). This assay quantitatively measures cellular lactate dehydrogenase (LDH), a stable cytosolic enzyme that is released on cell lysis. LDH oxidises lactate into pyruvate, generating NADH, which is then used to convert a tetrazolium salt into a red formazan product. The amount of colour formed is proportional to the number of lysed cells. A standard curve for determination of cell numbers was constructed using cells seeded at $1.32x10^6$ cells/mm. Cells that remained alive by the end of the 3 day experiment were detached and lysed for the release of LDH, which was then measured. LDH activity was analyzed using the cytotoxicity detection kit and sample collection was performed according to the cytotoxicity kit manufacturer's instructions [48]. The absorbance

was measured on a Tecan plate reader at 490nm because it is considered proportional to the catalytic activity of LDH.

2.3.4 Statistical analysis

All the values of the fluorescence and absorbance measurements were obtained as means and standard error. The fluorescence and LDH absorbance were correlated with the extensively analysed topography of the surfaces to determine the parameters that have the highest influence on L929 cellular response. The model for the prediction of fluorescence and LDH absorbance was derived from the linear fit of the correlation sets according to the statistical model [49]:

$$y = \sum_{j=1}^{k} \beta_j x_j + \varepsilon, \qquad \text{Eqn 2}$$

Where y corresponds to the fluorescence or LDH absorbance and the dependent variable, x_j corresponds to the roughness parameter as the jth predictor, β_j is the jth regression coefficient, and ε is a random error. For each roughness parameter the correlation coefficients and standard deviations of the residual (i.e. modelled data minus experimental data) were computed. For comparison with cast specimen and identifying the fibroblast cell response to the surface roughness based on the SLM processing parameters, the software program Statease Design-Expert for Windows (version 6) was used to carry out the Analysis of variance (ANOVA) and independent sample T-test. Values of $p < 0.05$ were considered to be statistically significant to the cast Co-Cr-Mo and indicated by an asterisk (*).

3 Results

3.1 Surface characteristics

The least rough SLM surface was obtained on the vertical (90°) Co-Cr-Mo88 sample (Ra and Rq) as can be seen from the 2D amplitude surface characteristics in Table 2Table . There was also little variation in surface roughness between the horizontal (0°) and the inclined (55°) orientations at this low energy density. The highest value of the maximum profile peak height (Rp), highest maximum profile valley depth (Rv) and the highest value of the total profile height (Rt) were obtained from Co-Cr-Mo88 oriented at 0°. It can be seen from Table 2 that 2D amplitude parameters were considerably higher in SLM Co-Cr-Mo samples than on the cast surface.

Surface Parameter (μm)	Ra	Std Dev	Rq	Std Dev	Rp	Std Dev	Rv	Std Dev	Rt	Std Dev
CoCrMo88 – (0°)	29.25	11.35	38.95	14.97	101.54	49.99	-72.67	28.95	174.22	67.26
CoCrMo 88- (55°)	25.51	7.35	31.01	7.63	67.05	17.40	-71.66	6.31	138.72	22.65
CoCrMo 88 - (90°)	7.43	0.55	9.22	0.65	27.23	4.26	-17.08	1.75	44.31	4.82
CoCrMo 208 - (0°)	14.74	2.76	18.16	3.16	41.38	9.71	-42.21	3.38	83.59	12.10
CoCrMo 208 - (55°)	20.62	2.68	25.97	3.18	76.14	11.10	-54.59	8.40	133.71	14.72
CoCrMo 208 - (90°)	12.11	0.66	14.90	0.79	45.82	1.76	-33.65	4.29	79.47	4.49
CoCrMo Cast	4.32	0.94	5.12	1.39	16.04	7.25	-10.39	1.02	26.44	7.43

Table 2: 2D amplitude surface characteristics of the SLM and cast Co-Cr-Mo discs characterised through interferometry.

In order to attain a further understanding of the variation in surface roughness values obtained using white interferometry, the topographic 3D views of the SLM Co-Cr-Mo discs were studied and these are shown with their corresponding R_a values in Fig 2. In comparison, the 3D view for the cast Co-Cr-Mo sample is shown in Fig 4 (a) together with the corresponding R_a value. Furthermore, to understand the localised change of surface features with the SLM laser input energy parameters and part the orientation, the top surface structures of the SLM fabricated samples were investigated using SEM and compared to cast as shown in Fig 3 and Fig 4 (b). As mentioned earlier, it can be deduced from Table 2, Fig 2, Fig 3 and

Fig 4 that the selective laser melted specimens have a generally rougher surface in terms of the R_a value than their cast counterpart. This is due the presence of adherent unmelted powder particles and also due to track or hatch patterns as shown in Fig 3.

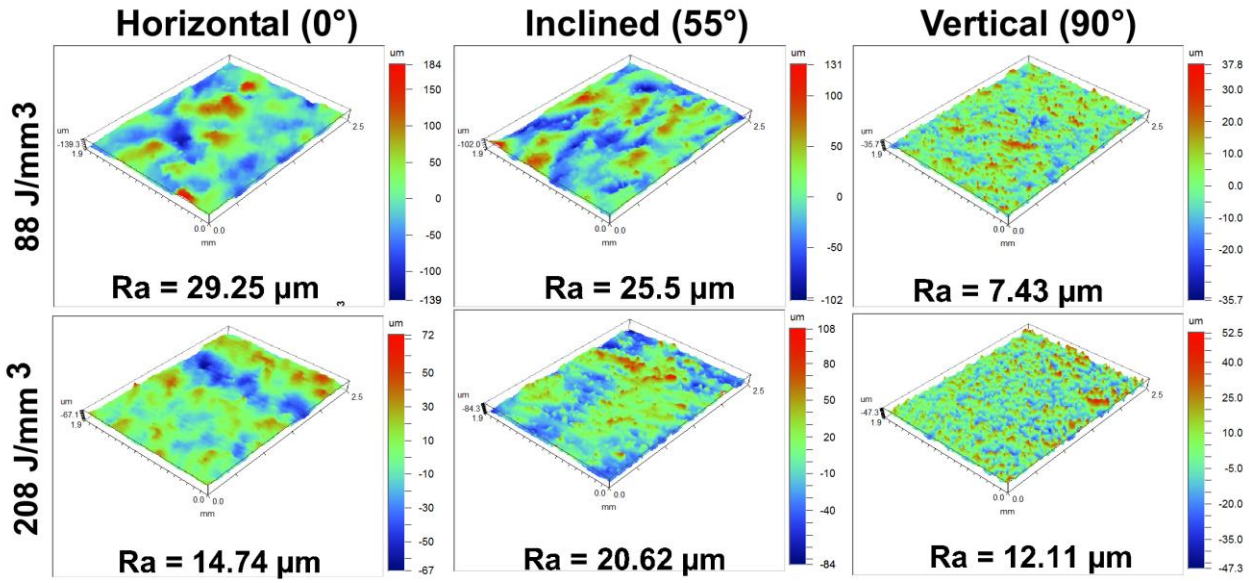

Fig 2: Topographic 3D view of SLM Co-Cr-Mo horizontal (0º), inclined (55º) and vertical (90º) surfaces showing corresponding R_a values for different part orientations and volumetric laser energy densities.

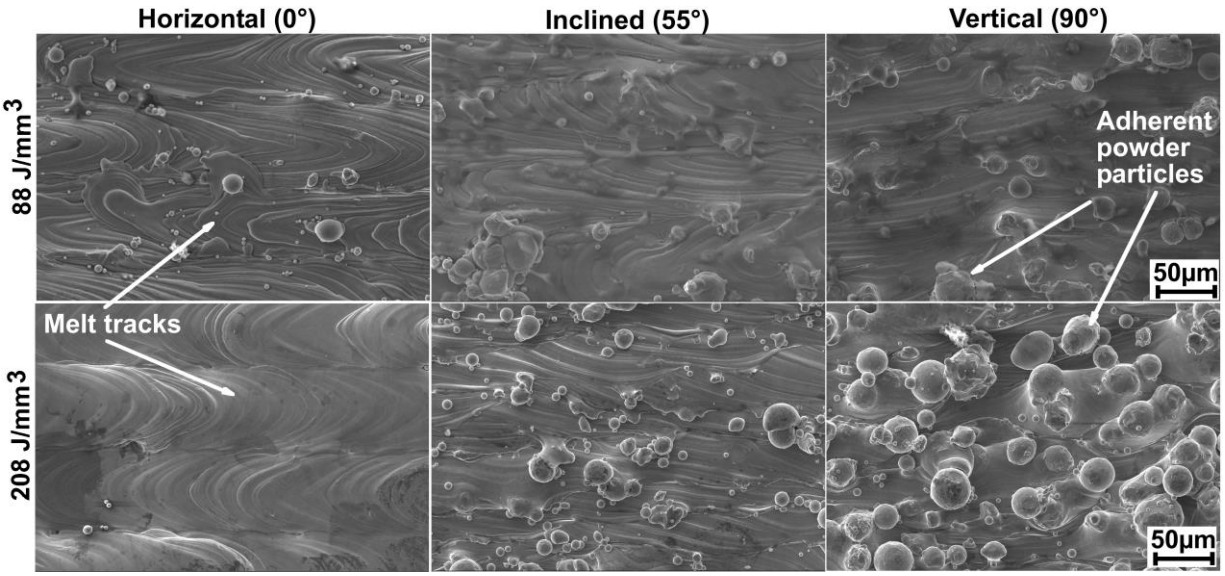

Fig 3: SEM local surface topography comparing the horizontal (0º), inclined (55º) and vertical (90º) SLM Co-Cr-Mo surfaces compared with different volumetric laser energy densities (before cell culture).

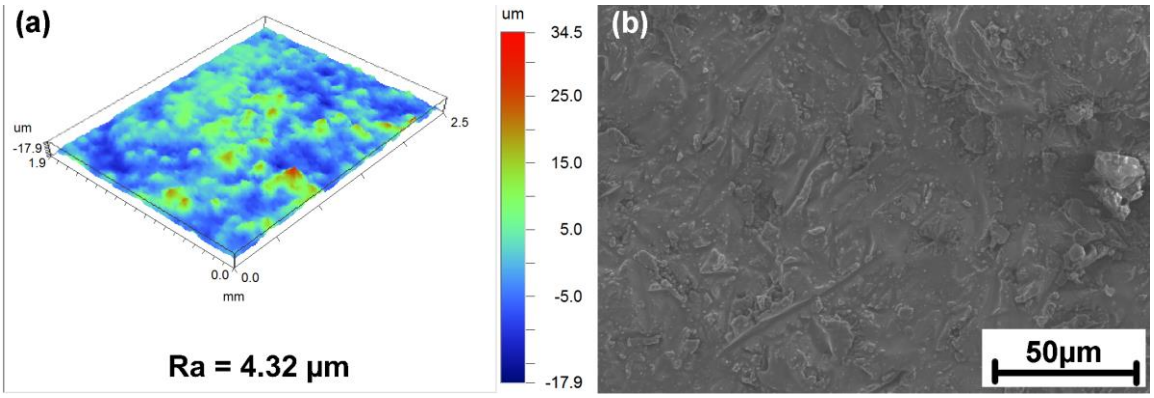

Fig 4: Co-Cr-Mo cast surfaces illustrated through 3D topographic view and SEM, before cell culture.

Fig 3 shows larger areas on the horizontal (0°) surface in both laser energy samples dominated by melt pool and laser tracks and this illustrates the nature of the SLM process where the laser scanning is performed line by line and the laser energy causes melting along a row of powder particles, forming a continuous liquid scan track in a cylindrical shape [35]. At the increased laser energy density of 208 J/mm^3, the melt tracks were found to be more continuous with less turbulent zones. The inclined (55°) sample surfaces at both laser energy densities showed a combination of adherent unmelted and completely melted powder particles as a result of decreased surface energy of up until the final equilibrium state through the breaking up of the melt track into several metallic agglomerates in spherical shape [50]. In the vertical, the density of unmelted non adherent particles was found to be increased on the Co-Cr-Mo208 than on the Co-Cr-Mo88 sample. The absence of adequate surface energy to melt the powders at the vertical (90°) orientation did not however contribute to a higher

surface roughness as the overall topography of the surface was stable. Whilst the average surface roughness measured over larger scan lengths (2.5 x 1.9 mm) showed that the horizontal surfaces had rougher topographies, the surface texture from SEM micrographs indicated that the powder particles on the horizontal surfaces had all the powder fully melted and were therefore considered to have smoother textures at the local fibroblast cell initial interaction and attachment regions.

3.2 **Cell proliferation and morphology**

Fig 5 shows SEMs of L929 mouse fibroblast cell growth on the SLM Co-Cr-Mo discs. The micrographs of L929 mouse fibroblast cultured on cast samples is shown for comparison in Fig 5 (a). The SEM micrographs show that the cells attached and spread well on all surfaces as it is expected that cells grow on biocompatible surfaces with passage of time. The cellular filopodia interaction of the L929 cells with the SLM is shown in higher magnification in Fig 5 (a, b,c,g,h,and i) and this shows the cells becoming more fibroblastic. The results in Fig 5 illustrate that the fibroblast cells were able to grow on all the SLM surfaces. It is not possible to make a comprehensive comparison of the cell proliferation and morphology based on the different surface topographies (hence SLM processing parameters) because the micrographs were taken at high resolution. However, Fig 5 (b and i) show that large steps can be overcome by the cells when they are able to form filapodial adhesion at the microlevel around surface features created by powder particles, illustrating that cells can use the edges of topographical features as footholds to gain mechanical adhesion [31]. The L929 cells showed typical filamentous morphology of L929 fibroblasts, creating bridges between surface features created by the powder morphology and hatch patterns of the SLM process and lengthening overall and over a greater surface area. Overall, the cells displayed a morphology that is expected with the L929 cell line, exhibiting cellular protrusions extending from the cellular

periphery and cell-cell contacts. In comparing the SLM Co-Cr-Mo cell growth to the reference cast sample, it was found that the cell distribution was homogenous, and cells appeared to cover as much area of the sample area on the cast sample despite the different surface topography. Further investigations were carried out by analysing the stained nuclei and F-actin patterns of L929 cells since focal contacts of cells have an important role in cell alignment to surface topography through influence on the actin cytoskeleton [30].

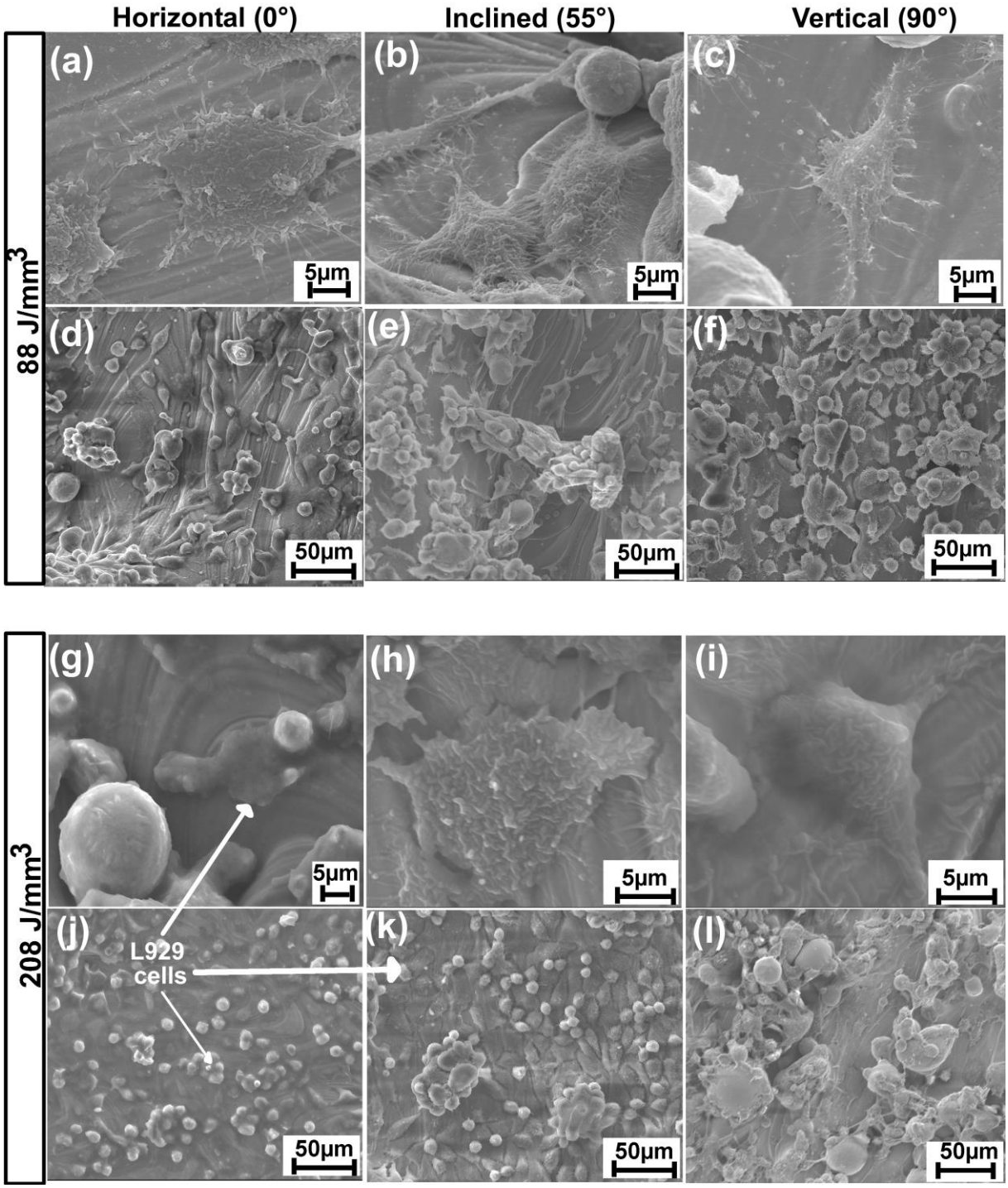

Fig 5: Scanning electron micrographs of L929 mouse fibroblast cells cultured on horizontal (0°), inclined (55°) and vertical (90°) SLM Co-Cr-Mo and reference cast discs for 3 days. The cellular filopodia interaction of the L929 cells with the SLM is shown in higher magnification in (a, b,c,g,h,and i)

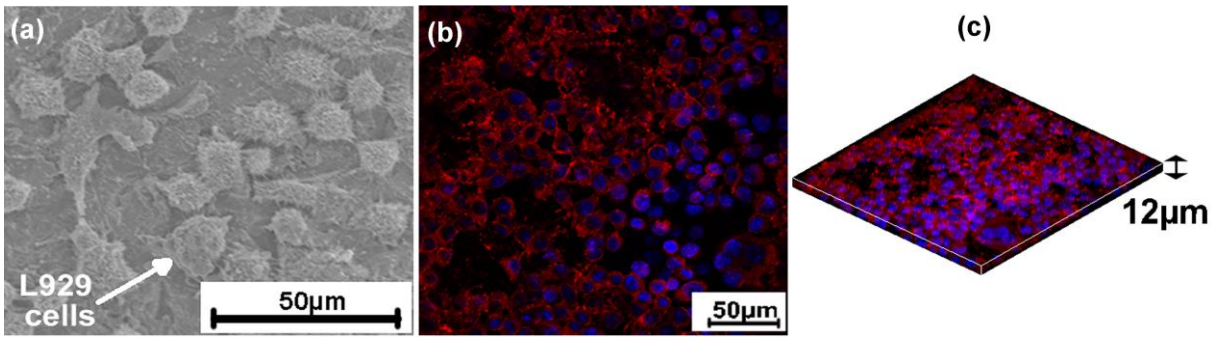

Fig 6: Scanning electron micrographs of L929 mouse fibroblast cells (a) and stained nuclei and F-actin patterns of L929 cell (b) and 3D projection of the cells (c) cultured on cast samples.

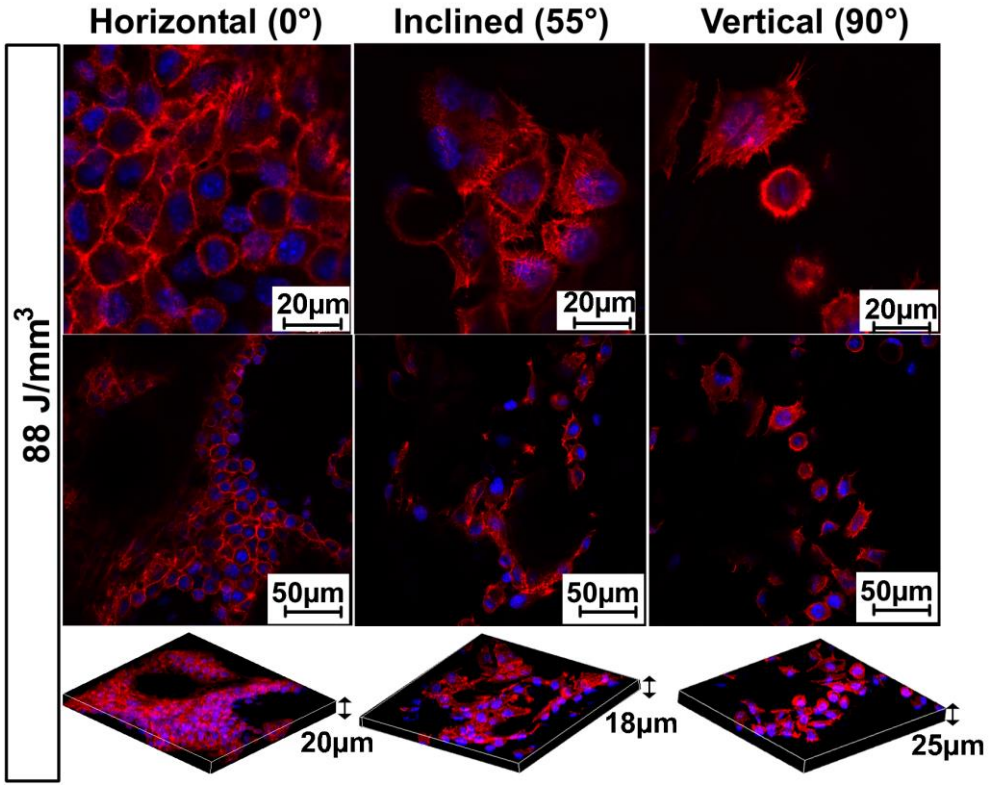

Fig 7: Stained nuclei and F-actin patterns of L929 cells and 3D projection of the cells cultured for 3 days on the 88 J/mm^3 SLM Co-Cr-Mo samples.

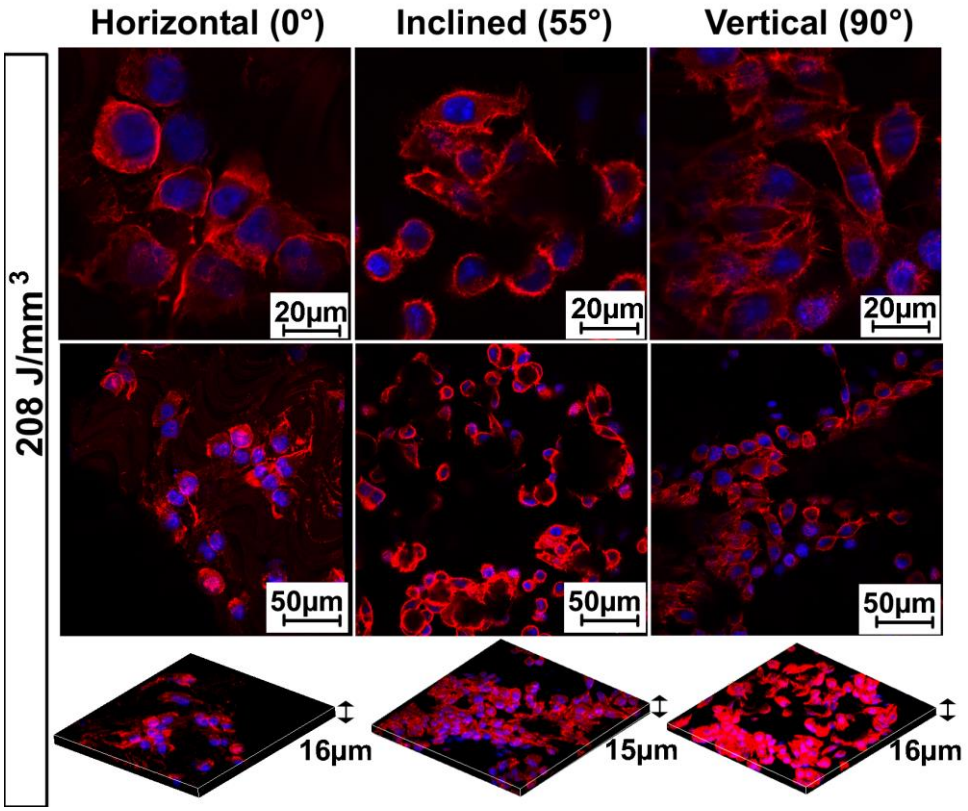

Fig 8: Stained nuclei and F-actin patterns of L929 cells cultured for 3 days on the 208 J/mm^3 SLM Co-Cr-Mo samples.

Fig 7 shows stained nuclei (blue) and F-actin (red) patterns of L929 cells cultured for 3 days on the SLM Co-Cr-Mo. The results for the cast samples are shown for comparison in Fig 6(b). Cell cytoskeletal staining of F-actin and nuclei are shown to follow outlines representative of groves and powder features. Fig 7 and Fig 8 show in more detail the type of cell/topography interaction revealed by SEMs analysis. It can be seen from Fig 7 and Fig 6 (b) that the volume of cells on the cast sample appeared to be higher due to the more regular (flatter) nature of the surface topography. In all relatively rough SLM surface, the cells displayed cytoskeletal actin organisation that is consistent with L929 cells on irregular implant surfaces. The SLM samples showed that cells were proliferate in deep lying regions of the rough surfaces. Thus, the nuclei staining showed round irregular distribution which is also consistent with the SLM Co-Cr-Mo surfaces and the 2 dimensional study of the samples

showed the concentration of cells on the surface which revealed the growth of the cells around the powder particle profiles. The 3D projections of the stained nuclei and F-acting patterns showed that cell growth was in all directions cell but growth was irregular. It is expected that after a longer passage of time than the three days for which the cells were cultured, the cells will appear regular as they proliferate across the Co-Cr-Mo and it is also worth mentioning that the 3D projection sampling was relatively small when taking into consideration topographical features of the SLM surfaces.

3.3 Cell Viability and cytotoxicity

Fig 9 shows the results of fluorescence as a measure of the cell viability on three different orientations and two different input laser energy densities. After 3 days the metabolic activity on the SLM Co-Cr-Mo matched the cast on the Co-Cr-Mo208 horizontal (0°) and on the Co-Cr-Mo88 vertical (90°) samples and was higher on all the other SLM Co-Cr-Mo than on the cast sample. On the SLM samples where the number of cells detected was low the analysis of the error indicates that the data points were spread out over a wider range of values. The highest cell growth was detected on the CoCr-Mo88 horizontal (0°) and the Co-Cr-Mo208 inclined (55°) samples. Furthermore, a statistically significant difference ($p<0.05$) was found between the fluorescence measured on the Co-Cr-Mo88 horizontal (0°) SLM sample and reference cast ($p=0.008$) and also between Co-Cr-Mo208, inclined (55°) SLM and reference cast ($P=0.004$) as indicated by (*).

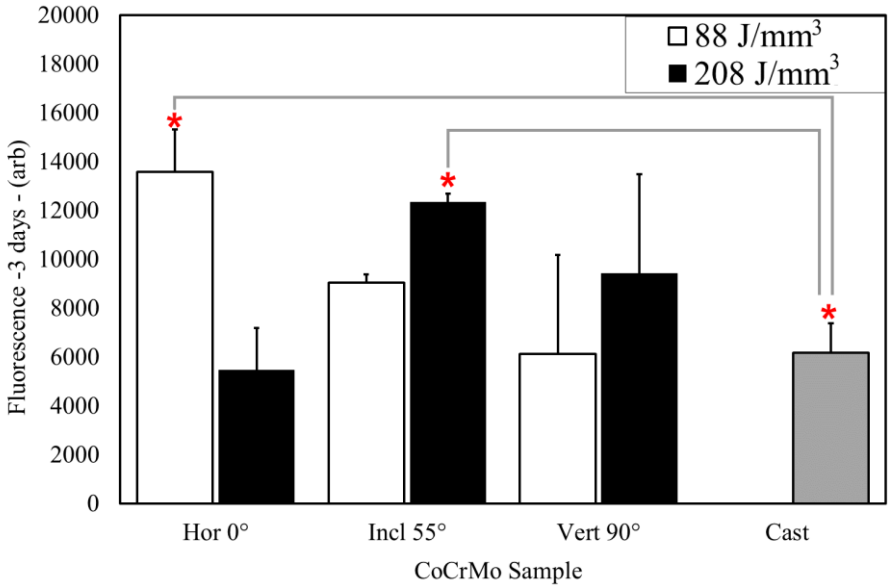

Fig 9: Cell viability on the different build orientation SLM Co-Cr-Mo disc samples (n=12) after 3 days. Fluorescence measured at 590 nm. *$p \leq 0.05$ relative to reference cast surface.

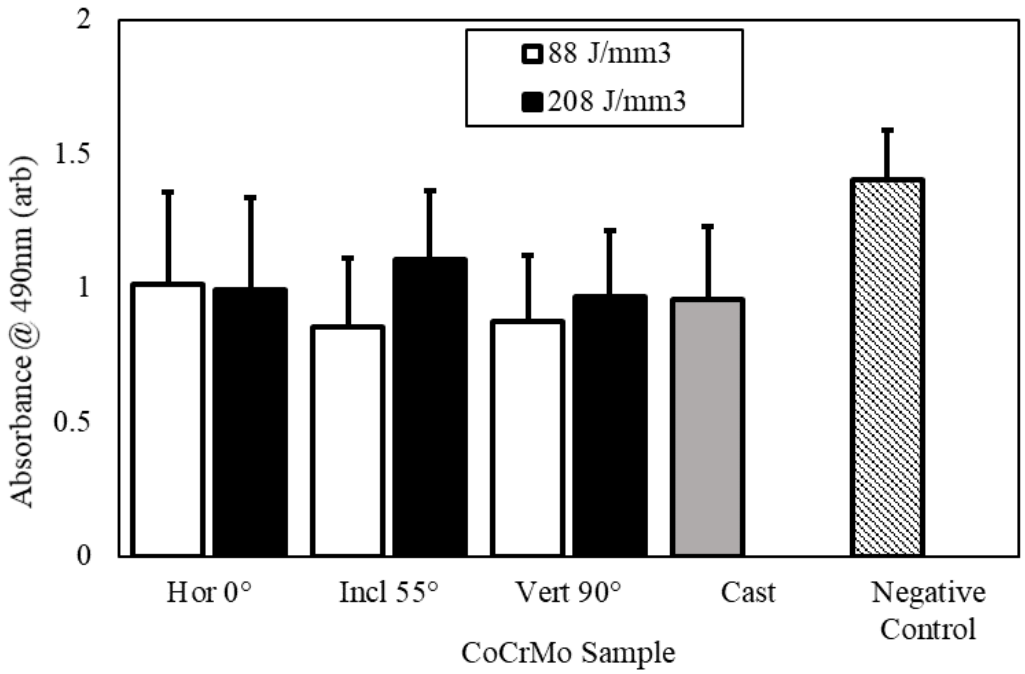

Fig 10: Cytotoxicity of SLM Co-Cr-Mo disc sample (n=6) results measured at 490 nm after 3 days incubation days.

Fig 10 shows the cytotoxicity of SLM Co-Cr-Mo disc samples results measured at 490 nm after 3 days incubation days. The amount of LDH released is proportional to the number of dead cells, which is quantified through a colorimetric assay by measuring the absorbance at 490 nm. The absorbance value reported in this study was calculated using the LDH released from the cells in the Co-Cr-Mo medium (after they were lysed). Therefore the number of cells detected via LDH release amongst all the SLM Co-Cr-Mo discs did not exhibit any negative cytotoxic effect. The reference cast Co-Cr-Mo discs did not reveal a significant detection of more cells than all of the SLM implants. The results are in agreement with those of the findings of the cell viability studies (Fig 9) in terms of cell count with SLM processing parameters (changing laser density and also increasing angle of orientation). In comparison to the negative control, the absorbance measurements on the Co-Cr-Mo samples were in the range of 60 to 80% of the control and comparable to cast. There was no statistical significance between any of the samples of the absorbance measured on all the surfaces.

3.4 Relationship between topography and biocompatibility

As mentioned in the earlier sections, the biocompatibility was characterised through cell viability and cytotoxicity measurements and the fluorescence and LDH absorbance were correlated with the extensively analysed topography of the surfaces. The best quantitative correlation between biocompatibility and the topography induced by processing parameters was found between the 3 days cultured fluorescence/LDH absorbance and the R_p value (the largest peak deviation of the roughness profile from the mean line within a sampling length) as shown in Fig 11 (a) and Fig 11 (b). For all the relations in Fig 11 (a) and Fig 11 (b), the lower the standard deviation of residuals and the higher the correlation coefficients, the more influential was the roughness parameter. This analysis shows that the amplitude parameters discriminated cell viability and cytotoxicity better, confirming that fibroblast cell growth after

3 days on SLM surfaces was more influenced by the amplitude rather than the functional (organisation and morphology) of the surface. The corresponding influential SLM processing parameters that are influential on the surface roughness values are shown in Table 2. The mechanisms which influenced cell growth on the various SLM surface topographies are explained above in terms of the cell morphology and quantitative viability and cytotoxicity results.

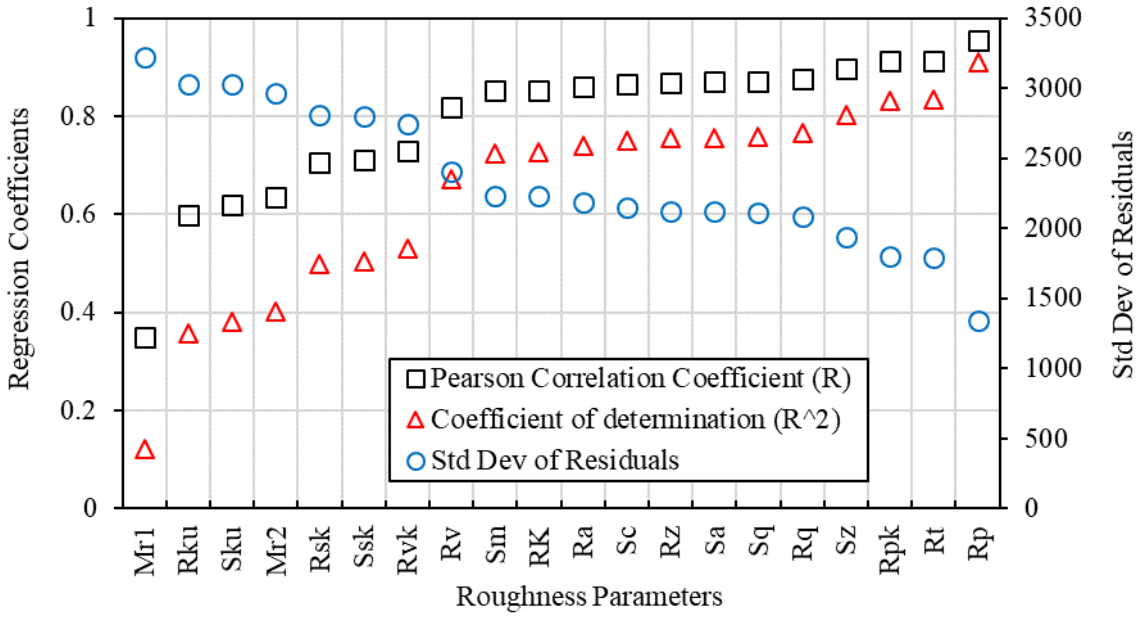

Fig 11: Relevance of the 20 surface roughness parameters when assessed for correlation with the measured fluorescence on the L929 fibroblast cells. The lower standard deviation of the residuals indicates the higher correlation of the parameter with the fluorescence measured.

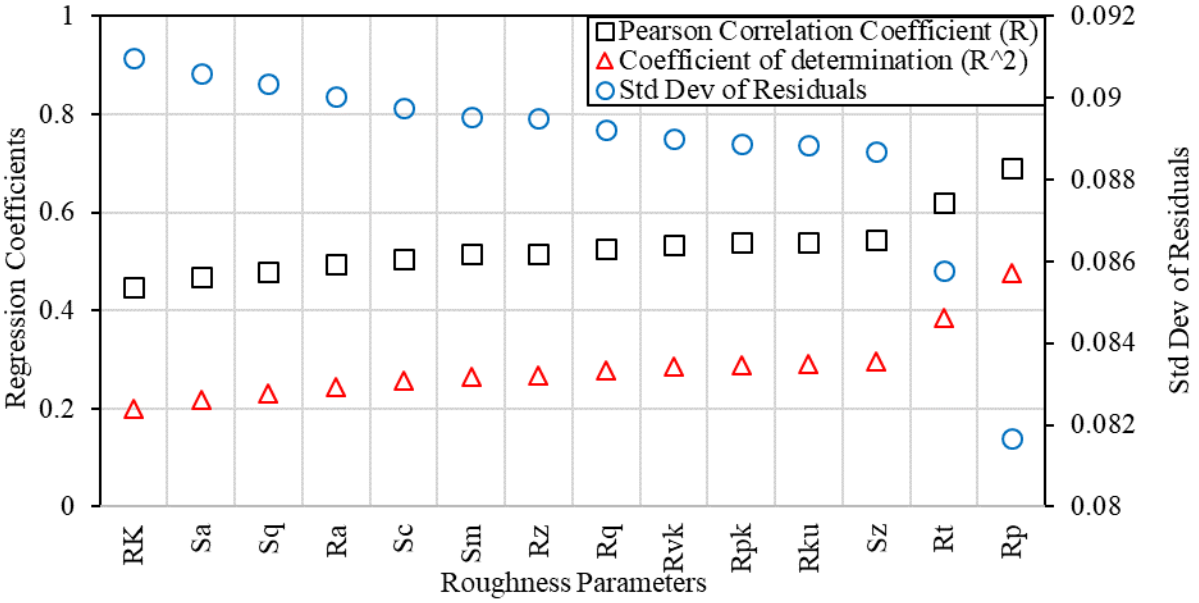

Fig 12: Relevance of the 14 surface roughness parameters when assessed for correlation with the measured LHD absorbance of the L929 fibroblast cells. The lower standard deviation of the residuals indicates the higher correlation of the parameter with the LDH absorbance measured.

4 Discussion

In this study, *in vitro* biocompatibility studies enabled the evaluation of the mouse fibroblast cells across a range of SLM Co-Cr-Mo surfaces, and provided an initial indication of how cells may behave *in vivo*. This approach is advantageous in that it reduces the time and cost for surface selection during medical device development. Separately, there is an increasing emphasis of alternative methods to animal models for materials screening [51]. It is appreciated however that the results from highly controlled *in vitro* studies have limitations in terms of being transferrable to the complex *in vivo* environment because various stimuli related to the topography and chemistry may compete with the surface characteristics provided by a biomaterial [30,52]. In this study, the variation of the processing parameters

were used to study the surface characteristics and their effect on the *in-vitro* biocompatibility of the SLM Co-Cr-Mo alloy.

The effect of SLM part orientation on the surface roughness has been attributed to the pattern of thermal history in different areas of the part which takes place during the layer to layer processing [53]. When the disc parts were oriented vertically (90°), they effectively consisted of smaller cross sections in comparison to the horizontal (0°) and the inclined (55°) samples. Therefore the vertical discs retained heat during the processing because the time for laser beam travel the cross section was shorter. Surfaces which retain heat may be beneficial for the wetting and spreading of molten material and thus for suppressing development of large cracks which are believed to be extremely harmful for porosity development within bulk samples [53] [54] and therefore surface roughness.

Consequently, there was improvement of surface characteristics in samples fabricated using a laser energy density of 208 J/mm^3 apart from the vertical specimens. Heterogeneous topographies on the Co-Cr-Mo discs were achieved as a result of the anisotropic character of the layer by layer generation process [55,56]. The vertical (90°) orientation SEM micrographs shown in Fig 3 indicate that there was a larger volume of more densely populated partial melted adherent particles as a direct result of the lack of exposure to the beam and thermal history. On the other hand the average roughness (R_a and R_q) values measured over a larger scan lengths (2.5 x 1.9 mm) were lower because the layering was more stable resulting in the surface equilibrium in contrast to the horizontal (0°) and inclined (55°) where there were turbulent zones created by unstable melt tracks. On the SLM system, the actual melting and welding together of powder particles takes place on the horizontal plane which results sputtering and rougher surface if the key parameters which are used to melt the

powder are not optimised. SEM analysis of the inclined (55°) orientation part results showed that the volume of partially melted particles was reduced because beam energy per unit volume was increased. When comparing the interferometry results of the SLM discs, the vertical (90°) samples at both laser energy densities, had a smallest value of the maximum profile depth (R_v) also due to the absence of the turbulent action of the laser beam in melting of powder particles.

The different surface features in this work have been shown to promote metabolic activity in slightly varying degrees. The 88 J/mm^3 horizontal (0°) and 208 J/mm^3 inclined (55°) samples had the highest number of cells counted by means of the fluorescence. The results show that the microscale surface properties can affect the mass transport ability, influencing cell attachment and growth on an implant's surface. This highlights the greater sensitivity of mouse fibroblast cells to changes in surface environment and potentially mechanisms for tissue regeneration. These mechanisms are the way in which cells respond to the topography by adjusting adhesion, migration, morphology, cytoskeleton [30].

The quantitative results based on optical density have not revealed any significant advantage of the cast Co-Cr-Mo implant in comparison to SLM Co-Cr-Mo implants based on the difference of the surface topography. This is despite the fact that it was expected for rougher SLM Co-Cr-Mo surface topographies to have an increased surface area compared to the relatively smoother topographies and the reference cast. The biocompatibility assessment in many cases report that more protein may adsorbed in rough surfaces [30]. The cast sample was tested "as cast" and without any post processing. It is occasional practice that cast Co-Cr-Mo the alloy is post-processed by hot isostatic pressing and subsequently heat-treated [3]. Therefore, examination of the factors that affect cell growth, particularly the attachment and

proliferation of cells on the Co-Cr-Mo surfaces has shown that the rough surfaces could support cell attachment and proliferation, as well as on homogeneous surface samples such as cast Co-Cr-Mo. Generalisation of the results obtained in this study is however complicated by conflicting reports. Several reports describe increased proliferation and osseointegration on micron-scale features compared to smooth controls, whereas others report no difference or the opposite trend for cobalt chromium [57-59,30].

The in-vitro biocompatibility on SLM surfaces was more influenced by the amplitude than by the organisation and spatiality of the surface. The larger peaks led to a consistent proliferation and attachment of cells in comparison by physically constraining cells until they were able to elongate and spread further across the surface [30,60] [61]. The constraining is linked to the local adhesion mechanisms of cells which have been reported to affect the cell cytoskeleton depending on the size of the grooves [62,63]. The reason for this is that at micron-scale heights similar to that of the cell, the cells are forced to orient to the features where the small cells are guided by features present [31]. Furthermore the SLM surface is very much dominated either by melt tracks or by powder shape, steep or round peaks but these have been shown not to reduce the number of contact points or weaken adhesion significantly as has been reported in other studies as demonstrated in Fig 5 (b and i) [30].

It appears that different surface topography affects protein adsorption in different ways, and the inconsistencies in reported results suggest that comprehensive understanding of this phenomenon is some way off. The surface chemistry is also known to affect cell behavior but in this study it has been assumed that there is little variation on the SLM Co-Cr-Mo and the fact that it is desirable to reduce the experimental parameters by having the cells exposed to only one chemistry has been taken into consideration [30]. However, further studies should be carried out to find out whether the SLM process results in inadvertent chemical patterning

when melting Co-Cr-Mo because in other studies it has been suggested that the amount of metal elution from Co-Cr-Mo could be closely related to the microstructure formed by the SLM process [4].

5 Conclusion

In this study Co-Cr-Mo discs with different surface topographies were successfully built using the SLM technique. The different surface topographies obtained using different fabrication parameters revealed that the horizontal and inclined surfaces had higher R_a values due to overmelting and the effect of the input laser energy density whereas the vertical orientation had lower values of surface characterisation values due to stability of the layering. All samples supported the attachment and proliferation of L929 fibroblast cells during our experiments and were comparable to the reference cast surface which was more homogeneous and had the smoothest surface roughness complemented.

This study has demonstrated that SLM can be used successfully to manufacture safe, biocompatible Co-Cr-Mo alloy structures for use as medical devices in some applications. The process can be used in designing implants with specific surface roughnesses. The biocompatibility studies have shown how the design flexibility can be correlated with properties without significantly affecting the biocompatibility properties. This study has shown that there may be complexities associated with SLM implants and the cell attachment or bone ingrowth, for example, may be affected throughout a single Co-Cr-Mo device due to part orientation in build chamber because this is more influenced by the amplitude than by the morphology of the surface.

6 Acknowledgements

The author would like to sincerely thank Dr. Nicola Green at the Kroto Imaging Facility (University of Sheffield) for help with acquisition of images on the fluorescent microscope. The author would also like to thank the Wellcome Trust for providing financial support through the Institutional Strategic Support Fund (ISSF) at the University of Sheffield to conduct this research. Last but not least, appreciation also goes to Dr. Anthony Johnson and Paul V. Hatton from the School of Clinical Dentistry and also to Professor Iain Todd from the Department Materials Science and Engineering at the University of Sheffield for their discussions and assistance.

7 References

1. Lee S-H, Nomura N, Chiba A (2008) Significant improvement in mechanical properties of biomedical Co-Cr-Mo alloys with combination of N addition and Cr-enrichment. Mater Trans 49 (2):260-264. doi:https://doi.org/10.2320/matertrans.MRA2007220

2. Shah FA, Omar O, Suska F, Snis A, Matic A, Emanuelsson L, Norlindh B, Lausmaa J, Thomsen P, Palmquist A (2016) Long-term osseointegration of 3D printed CoCr constructs with an interconnected open-pore architecture prepared by electron beam melting. Acta Biomater 36:296-309. doi:https://doi.org/10.1016/j.actbio.2016.03.033

3. Hedberg YS, Qian B, Shen Z, Virtanen S, Odnevall Wallinder I (2014) In vitro biocompatibility of CoCrMo dental alloys fabricated by selective laser melting. Dental Materials 30 (5):525-534. doi:https://doi.org/10.1016/j.dental.2014.02.008

4. Takaichi A, Suyalatu, Nakamoto T, Joko N, Nomura N, Tsutsumi Y, Migita S, Doi H, Kurosu S, Chiba A, Wakabayashi N, Igarashi Y, Hanawa T (2013) Microstructures and mechanical properties of Co-29Cr-6Mo alloy fabricated by selective laser melting process for dental applications. J Mech Behav Biomed 21:67-76. doi:https://doi.org/10.1016/j.jmbbm.2013.01.021

5. Sidambe AT (2014) Biocompatibility of Advanced Manufactured Titanium Implants-A Review. Materials 7 (12):8168-8188. doi:https://doi.org/10.3390/ma7128168

6. Andani MT, Shayesteh Moghaddam N, Haberland C, Dean D, Miller MJ, Elahinia M (2014) Metals for bone implants. Part 1. Powder metallurgy and implant rendering. Acta Biomater 10 (10):4058-4070. doi:https://doi.org/10.1016/j.actbio.2014.06.025

7. Ivanova O, Williams C, Campbell T (2013) Additive manufacturing (AM) and nanotechnology: promises and challenges. Rapid Prototyping J 19 (5):353-364. doi:https://doi.org/10.1108/Rpj-12-2011-0127

8. van Noort R (2012) The future of dental devices is digital. Dent Mater 28 (1):3-12. doi:https://doi.org/10.1016/j.dental.2011.10.014

9. Harrison NJ, Todd I, Mumtaz K (2015) Reduction of micro-cracking in nickel superalloys processed by Selective Laser Melting: A fundamental alloy design approach. Acta Materialia 94:59-68. doi:https://doi.org/10.1016/j.actamat.2015.04.035

10. Vora P, Mumtaz K, Todd I, Hopkinson N (2015) AlSi12 in-situ alloy formation and residual stress reduction using anchorless selective laser melting. Additive Manufacturing 7:12-19. doi:https://doi.org/10.1016/j.addma.2015.06.003

11. Gebhardt A, Schmidt FM, Hotter JS, Sokalla W, Sokalla P (2010) Additive Manufacturing by Selective Laser Melting The Realizer Desktop Machine and its application for the Dental Industry. Physcs Proc 5:543-549. doi:https://doi.org/10.1016/j.phpro.2010.08.082

12. Vandenbroucke B, Kruth JP (2007) Selective laser melting of biocompatible metals for rapid manufacturing of medical parts. Rapid Prototyping J 13 (4):196-203. doi:https://doi.org/10.1108/13552540710776142

13. Sinirlioglu M Rapid Manufacturing of Dental and Medical Parts via LaserCUSING® Technology using Titanium and CoCr Powder Materials. In: RapidTech 2009: US-Turkey Workshop on Rapid Technologies, 2009.

14. Kruth J-P, Vandenbroucke B, Vaerenbergh vJ, Naert I (2005) Rapid manufacturing of dental prostheses by means of selective laser sintering/melting. http://doc.utwente.nl/52914/1/Wa1025.pdf. Accessed 21 April 2018, 2018
15. Garg A, Lam JSL, Savalani MM (2015) Laser power based surface characteristics models for 3-D printing process. Journal of Intelligent Manufacturing:1-12. doi:https://doi.org/10.1007/s10845-015-1167-9
16. Koutiri I, Pessard E, Peyre P, Amlou O, De Terris T (2018) Influence of SLM process parameters on the surface finish, porosity rate and fatigue behavior of as-built Inconel 625 parts. J Mater Process Tech 255:536-546. doi:https://doi.org/https://doi.org/10.1016/j.jmatprotec.2017.12.043
17. Mengucci P, Gatto A, Bassoli E, Denti L, Fiori F, Girardin E, Bastianoni P, Rutkowski B, Czyrska-Filemonowicz A, Barucca G (2017) Effects of build orientation and element partitioning on microstructure and mechanical properties of biomedical Ti-6Al-4V alloy produced by laser sintering. J Mech Behav Biomed 71:1-9
18. Zhang B, Huang QR, Gao Y, Luo P, Zhao C (2012) Preliminary study on some properties of Co-Cr dental alloy formed by selective laser melting technique. J Wuhan Univ Technol 27 (4):665-668. doi:https://doi.org/10.1007/s11595-012-0525-0
19. Strietzel R (2010) Selective Laser Melting in Dentistry. Informatics in Oral Medicine: Advanced Techniques in Clinical and Diagnostic Technologies: Advanced Techniques in Clinical and Diagnostic Technologies:111. doi:https://doi.org/10.4018/978-1-60566-733-1.ch008
20. ASTM (2012) Standard Specification for Cobalt-28 Chromium-6 Molybdenum Alloy Castings and Casting Alloy for Surgical Implants (UNS R30075). ASTM F75-12. American Society for Testing and Materials (ASTM) International, West Conshohocken, PA. doi:https://doi.org/10.1520/F0075-12
21. ISO (2016) Dentistry — Metallic materials for fixed and removable restorations and appliances. ISO 22674-16. International Organisation for Standardisation (ISO), Geneva

22. ASTM (2014) New Specification for Additive Manufacturing Cobalt-28 Chromium-6 Molybdenum Alloy (UNS R30075) with Powder Bed Fusion. ASTM WK51329. American Society for Testing Materials (ASTM) International, West Conshohocken, PA.
23. FDA (2016) Technical Considerations for Additive Manufactured Devices Draft Guidance. Food and Drug Administration. http://www.fda.gov/downloads/MedicalDevices/DeviceRegulationandGuidance/GuidanceDocuments/UCM499809.pdf. Accessed 21 April 2018, 2018
24. Inovar Communications Ltd (Metal AM) (2015) Additive Manufacturing in dental technology: Concept Laser enables the industrial manufacturing of dental implants at Fresdental. Innovar. http://www.metal-am.com/additive-manufacturing-in-dental-technology-concept-laser-enables-the-industrial-manufacturing-of-dental-implants-at-fresdental/. Accessed 21 April 2018, 2018
25. Jevremovic D, Kojic V, Bogdanovic G, Puskar T, Eggbeer D, Thomas D, Williams R (2011) A selective laser melted Co-Cr alloy used for the rapid manufacture of removable partial denture frameworks - initial screening of biocompatibility. J Serb Chem Soc 76 (1):43-52. doi:https://doi.org/10.2298/Jsc100406014j
26. Xin XZ, Xiang N, Chen J, Wei B (2012) In vitro biocompatibility of Co-Cr alloy fabricated by selective laser melting or traditional casting techniques. Mater Lett 88:101-103. doi:https://doi.org/10.1016/j.matlet.2012.08.032
27. Puskar T, Jevremovic D, Williams R, Eggbeer D, Vukelic D, Budak I (2014) A Comparative Analysis of the Corrosive Effect of Artificial Saliva of Variable pH on DMLS and Cast Co-Cr-Mo Dental Alloy. Materials 7 (9):6486-6501. doi:https://doi.org/10.3390/ma7096486
28. Hedberg Y, Odnevall Wallinder I (2014) Metal release and speciation of released chromium from a biomedical CoCrMo alloy into simulated physiologically relevant solutions. J Biomed Mater Res B 102 (4):693-699. doi:https://doi.org/10.1002/jbm.b.33048

29. Stanford CM (2008) Surface modifications of dental implants. Australian Dental Journal 53:S26-S33. doi:https://doi.org/10.1111/j.1834-7819.2008.00038.x

30. Kearns VR, McMurray RJ, Dalby MJ (2011) Biomaterial surface topography to control cellular response: technologies, cell behaviour and biomedical applications. In: Williams R (ed) Surface Modification of Biomaterials. Woodhead Publishing, pp 169-201. doi:https://doi.org/10.1533/9780857090768.1.169

31. Berry CC, Campbell G, Spadiccino A, Robertson M, Curtis ASG (2004) The influence of microscale topography on fibroblast attachment and motility. Biomaterials 25 (26):5781-5788. doi:https://doi.org/10.1016/j.biomaterials.2004.01.029

32. Brown B (2014) Characterization of 304L stainless steel by means of minimum input energy on the selective laser melting platform. Masters, Missouri University Of Science And Technology,

33. Simchi A, Pohl H (2003) Effects of laser sintering processing parameters on the microstructure and densification of iron powder. Mat Sci Eng A-Struct 359 (1–2):119-128. doi:https://doi.org/10.1016/S0921-5093(03)00341-1

34. Simchi A (2006) Direct laser sintering of metal powders: Mechanism, kinetics and microstructural features. Mat Sci Eng A-Struct 428 (1–2):148-158. doi:https://doi.org/10.1016/j.msea.2006.04.117

35. Gu D, Shen Y (2009) Balling phenomena in direct laser sintering of stainless steel powder: Metallurgical mechanisms and control methods. Mater Design 30 (8):2903-2910. doi:https://doi.org/10.1016/j.matdes.2009.01.013

36. Yang YQ, Lu JB, Luo ZY, Wang D (2012) Accuracy and density optimization in directly fabricating customized orthodontic production by selective laser melting. Rapid Prototyping J 18 (6):482-489. doi:https://doi.org/10.1108/13552541211272027

37. Yadroitsev I, Bertrand P, Smurov I (2007) Parametric analysis of the selective laser melting process. Appl Surf Sci 253 (19):8064-8069. doi:https://doi.org/10.1016/j.apsusc.2007.02.088

38. Sidambe AT, Todd I, Hatton PV (2016) Effects of build orientation induced surface modifications on the in vitro biocompatibility of electron beam melted Ti6Al4V. Powder Metall 59 (1):57-65. doi:https://doi.org/10.1080/00325899.2016.1153278
39. ISO (2009) Geometrical Product Specifications (GPS)-Surface Texture: Areal (Profile method-Terms, definitions and surface texture parameters). BS EN ISO 4287:1998 +A1:2009. International Organisation for Standardisation (ISO), Geneva
40. Precision_Device_Inc (1998) Surface Profile Parameters. Precision Devices Inc. https://www.scribd.com/document/257286818/Surface-Metrology-Guide-Profile-Parameters. Accessed 21 April 2018, 2018
41. ISO (2012) Geometrical Product Specifications (GPS)-Surface Texture: Areal (Part 2: Terms, definitions and surface texture parameters). BS EN ISO 25178-2:2012. International Organisation for Standardisation (ISO), Geneva
42. ASME_B46_Committee (2010) Surface Texture – Panel Discussion. Rensselaer. ftp://ftp.astmtmc.cmu.edu/docs/diesel/mack/minutes/2013/Mack.2013-02-07.Meeting/21763%20pdf.pdf. Accessed 21 April 2018, 2018
43. Stavroulakis P, Leach R (2016) Invited Review Article: Review of post-process optical form metrology for industrial-grade metal additive manufactured parts. Review of Scientific Instruments 87 (4):041101. doi:https://doi.org/10.1063/1.4944983
44. Anselme K, Bigerelle M (2006) Modelling approach in cell/material interactions studies. Biomaterials 27 (8):1187-1199. doi:https://doi.org/10.1016/j.biomaterials.2005.10.009
45. ASTM (2015) Standard Guide for Assessment of Surface Texture of Non-Porous Biomaterials in Two Dimensions. ASTM F2791-15. American Society for Testing Materials (ASTM) International, West Conshohocken, PA. doi:https://doi.org/10.1520/F2791-15
46. ISO (2009) Biological evaluation of medical devices. Part 5: Tests for in vitro cytotoxicity. ISO 10993-5:2009. International Organisation for Standardisation (ISO), Geneva

47. Samal SK, Dash M, Declercq HA, Gheysens T, Dendooven J, Van Der Voort P, Cornelissen R, Dubruel P, Kaplan DL (2014) Enzymatic mineralization of silk scaffolds. Macromol Biosci 14 (7):991-1003. doi:https://doi.org/10.1002/mabi.201300513

48. Promega_Corporation (2015) CytoTox 96® Non-Radioactive Cytotoxicity Assay Technical Bulletin. Promega. https://www.promega.co.uk/resources/protocols/technical-bulletins/0/cytotox-96-non-radioactive-cytotoxicity-assay-protocol/. Accessed 21 April 2018, 2018

49. Sidambe AT, Choong WL, Hamilton HGC, Todd I (2013) Correlation of metal injection moulded Ti6Al4V yield strength with resonance frequency (PCRT) measurements. Mat Sci Eng a-Struct 568:220-227. doi:https://doi.org/10.1016/j.msea.2013.01.040

50. Gu DD, Meiners W, Wissenbach K, Poprawe R (2012) Laser additive manufacturing of metallic components: materials, processes and mechanisms. Int Mater Rev 57 (3):133-164. doi:https://doi.org/10.1179/1743280411Y.0000000014

51. Stevenson G, Rehman S, Draper E, Hernandez-Nava E, Hunt J, Haycock JW (2016) Combining 3D human in vitro methods for a 3Rs evaluation of novel titanium surfaces in orthopaedic applications. Biotechnol Bioeng 113 (7):1586-1599. doi:https://doi.org/10.1002/bit.25919

52. Anselme K, Bigerelle M (2005) Topography effects of pure titanium substrates on human osteoblast long-term adhesion. Acta Biomater 1 (2):211-222. doi:https://doi.org/10.1016/j.actbio.2004.11.009

53. Qiu CL, Adkins NJE, Attallah MM (2016) Selective laser melting of Invar 36: Microstructure and properties. Acta Materialia 103:382-395. doi:https://doi.org/10.1016/j.actamat.2015.10.020

54. Mumtaz K, Hopkinson N (2009) Top surface and side roughness of Inconel 625 parts processed using selective laser melting. Rapid Prototyping J 15 (2):96-103. doi:https://doi.org/10.1108/13552540910943397

55. Ponader S, Vairaktaris E, Heinl P, Wilmowsky Cv, Rottmair A, Körner C, Singer RF, Holst S, Schlegel KA, Neukam FW, Nkenke E (2008) Effects of topographical surface

modifications of electron beam melted Ti-6Al-4V titanium on human fetal osteoblasts. J Bio Mater Res A 84A (4):1111-1119. doi:https://doi.org/10.1002/jbm.a.31540

56. Vaithilingam J, Prina E, Goodridge RD, Hague RJM, Edmondson S, Rose FRAJ, Christie SDR (2016) Surface chemistry of Ti6Al4V components fabricated using selective laser melting for biomedical applications. Mat Sci Eng C 67:294-303. doi:https://doi.org/10.1016/j.msec.2016.05.054
57. Stenlund P, Kurosu S, Koizumi Y, Suska F, Matsumoto H, Chiba A, Palmquist A (2015) Osseointegration Enhancement by Zr doping of Co-Cr-Mo Implants Fabricated by Electron Beam Melting. Additive Manufacturing 6:6-15. doi:https://doi.org/10.1016/j.addma.2015.02.002
58. Sing SL, An J, Yeong WY, Wiria FE (2016) Laser and electron-beam powder-bed additive manufacturing of metallic implants: A review on processes, materials and designs. Journal of Orthopaedic Research 34 (3):369-385. doi:https://doi.org/10.1002/jor.23075
59. Grandfield K, Palmquist A, Gonçalves S, Taylor A, Taylor M, Emanuelsson L, Thomsen P, Engqvist H (2011) Free form fabricated features on CoCr implants with and without hydroxyapatite coating in vivo: a comparative study of bone contact and bone growth induction. J Mater Sci: Mater Med 22 (4):899-906. doi:https://doi.org/10.1007/s10856-011-4253-3
60. Dalby MJ, McCloy D, Robertson M, Wilkinson CDW, Oreffo ROC (2006) Osteoprogenitor response to defined topographies with nanoscale depths. Biomaterials 27 (8):1306-1315. doi:https://doi.org/10.1016/j.biomaterials.2005.08.028
61. Ohara PT, Buck RC (1979) Contact guidance in vitro: A light, transmission, and scanning electron microscopic study. Experimental Cell Research 121 (2):235-249. doi:https://doi.org/10.1016/0014-4827(79)90002-8
62. den Braber ET, de Ruijter JE, Ginsel LA, von Recum AF, Jansen JA (1996) Quantitative analysis of fibroblast morphology on microgrooved surfaces with various groove and

ridge dimensions. Biomaterials 17 (21):2037-2044. doi:https://doi.org/10.1016/0142-9612(96)00032-4

63. Brunette DM (1986) Fibroblasts on micromachined substrata orient hierarchically to grooves of different dimensions. Experimental Cell Research 164 (1):11-26. doi:https://doi.org/10.1016/0014-4827(86)90450-7

Graphical Abstract

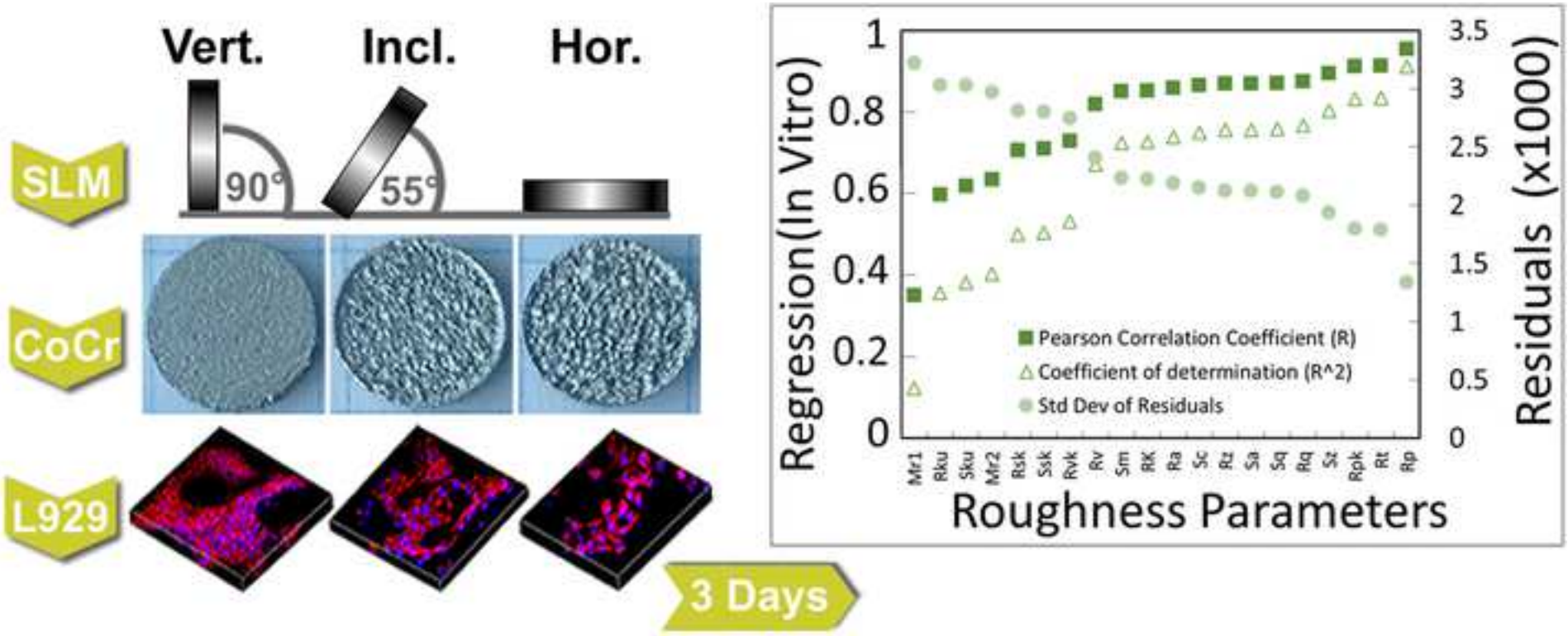

Figure 1 -CAD illustrations of the orientations of the Co-Cr-Mo

Click here to download Figure FIGURE~1.TIF

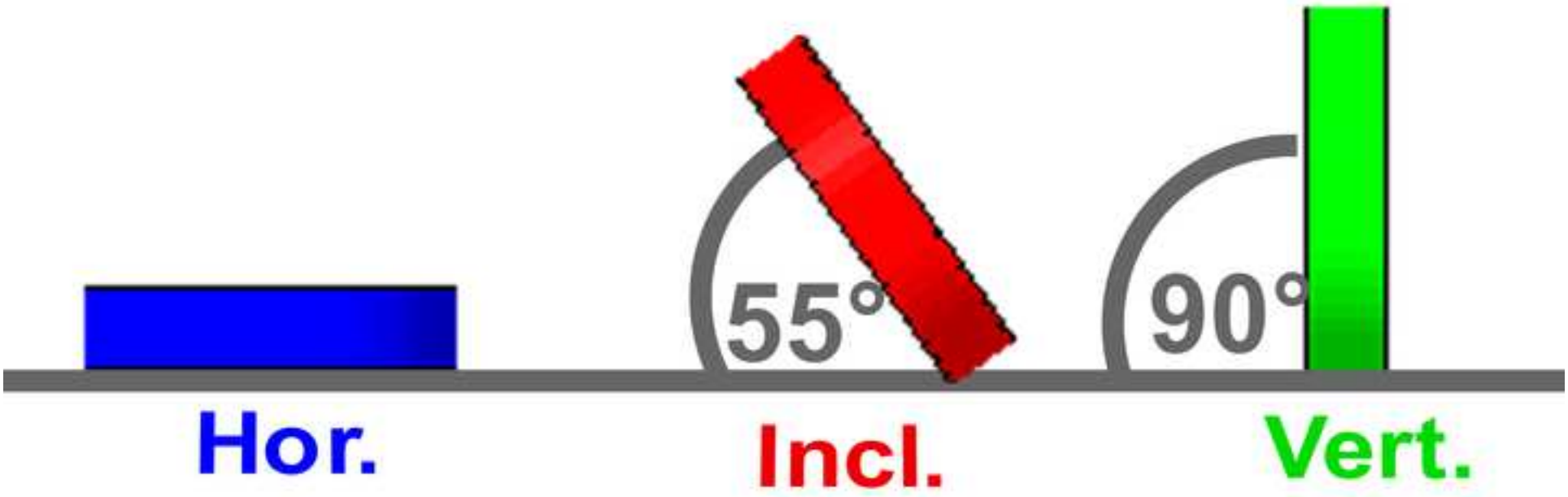

Figure 2 -Topographic 3D view of SLM Co-Cr-Mo

Click here to download Figure Figure 2 -Topographic 3D view of SLM Co-Cr-Mo.tif

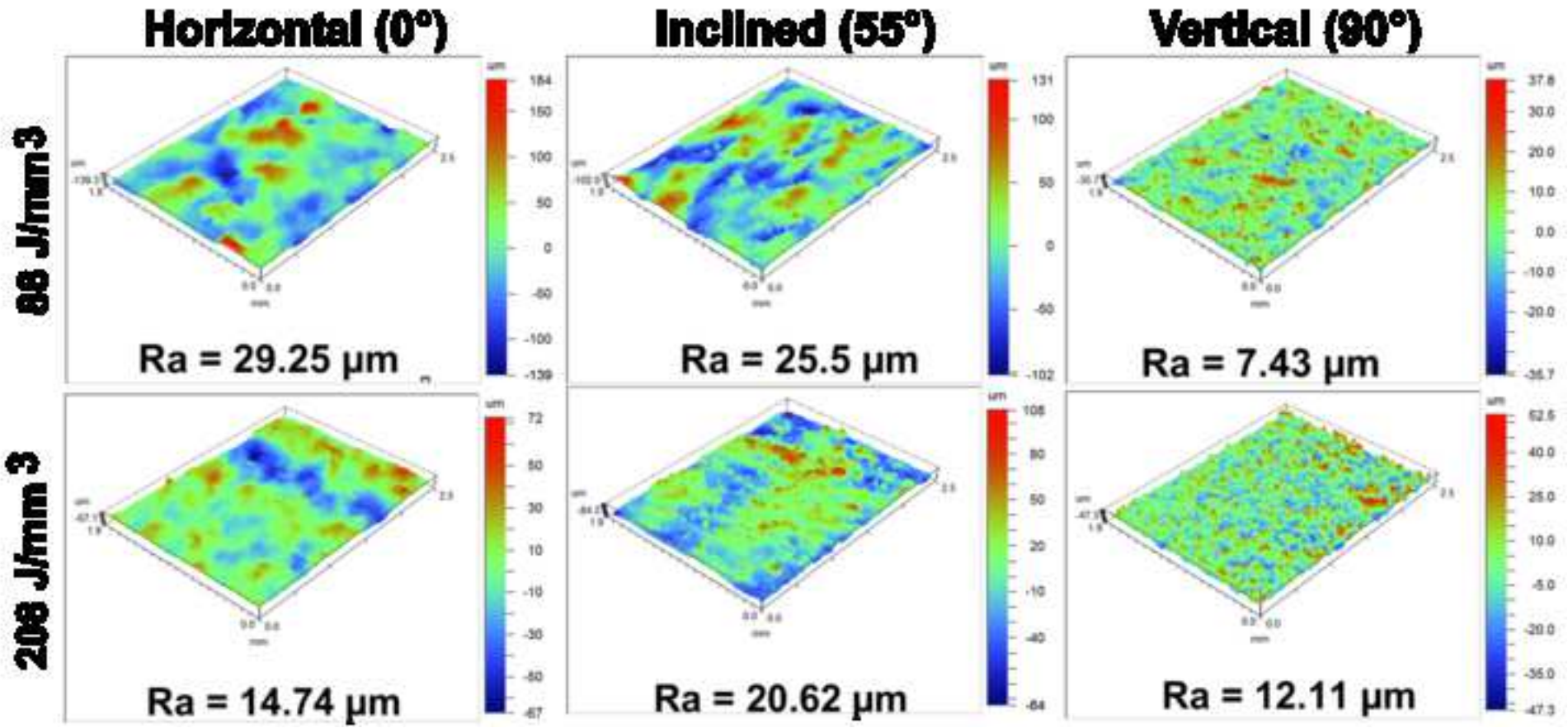

Figure 3 -SEM local surface topography

Click here to download Figure Figure 3 -SEM local surface topography.tif

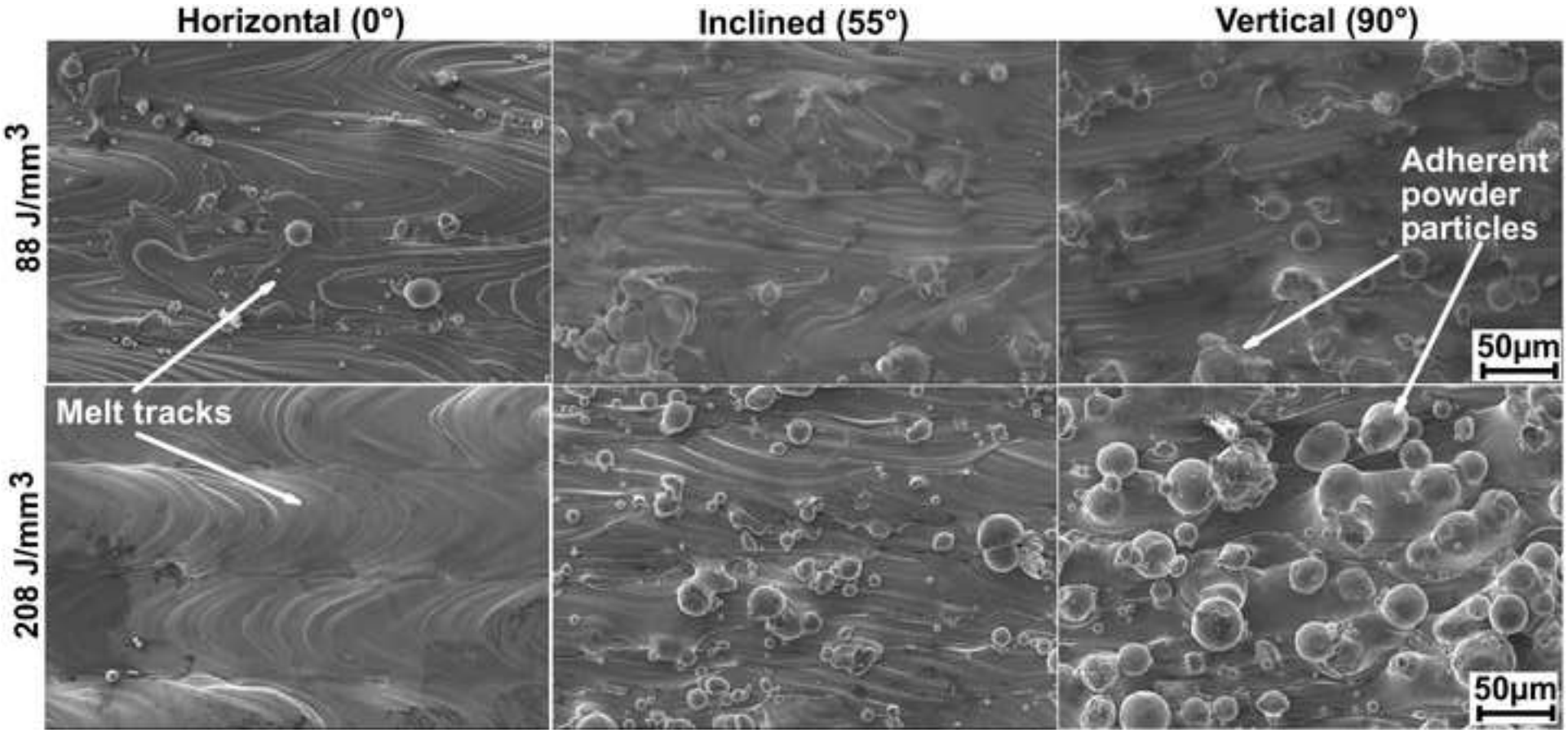

Figure 4 -Co-Cr-Mo cast surfaces 3D topographic view and SEM

Click here to download Figure FIGURE~4.TIF

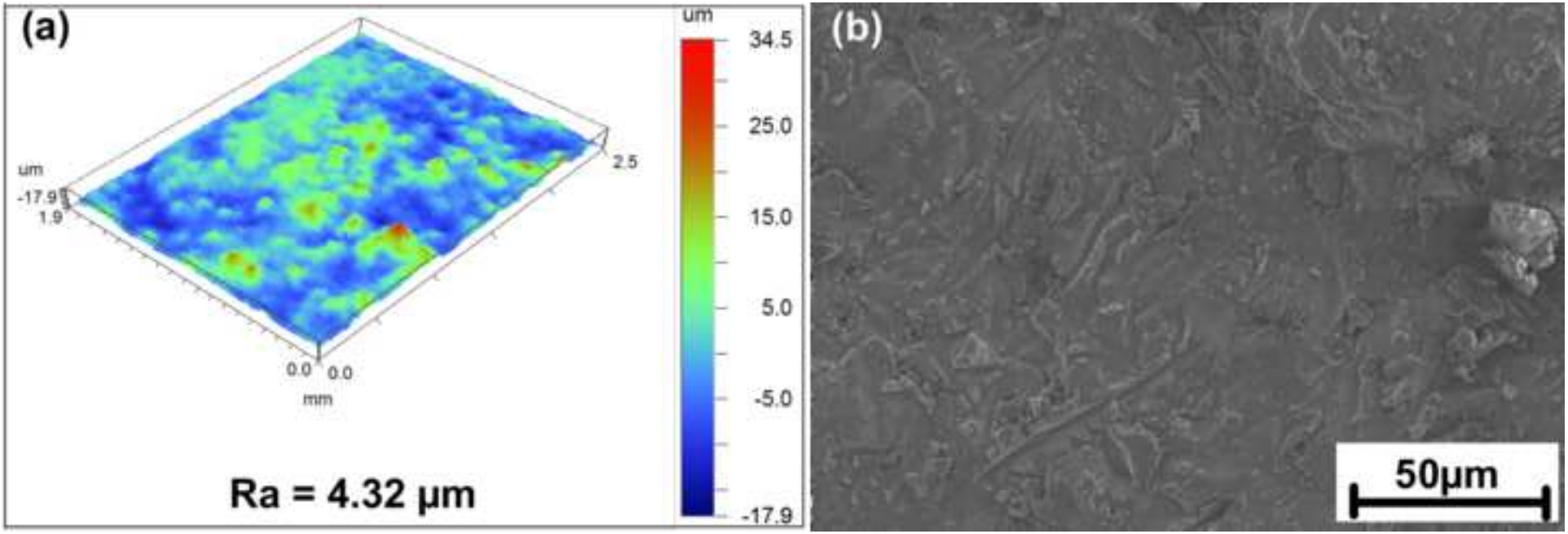

Figure 5 -Scanning electron micrographs of L929 mouse fibroblast cells

Click here to download Figure FIE20B~1.TIF

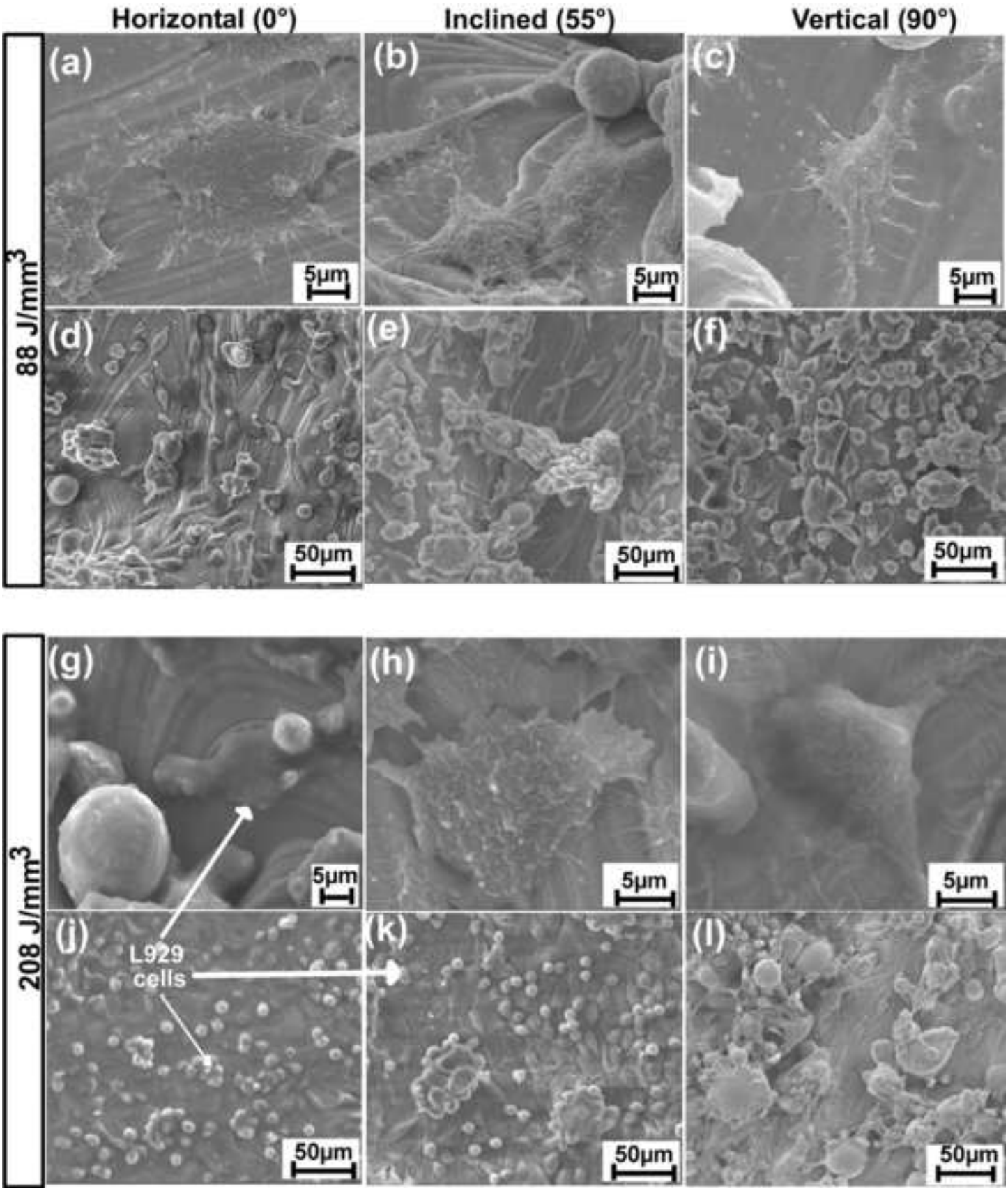

Figure 6 -Cast SEM of cells and stained nuclei and F-actin

Click here to download Figure FI6713~1.TIF

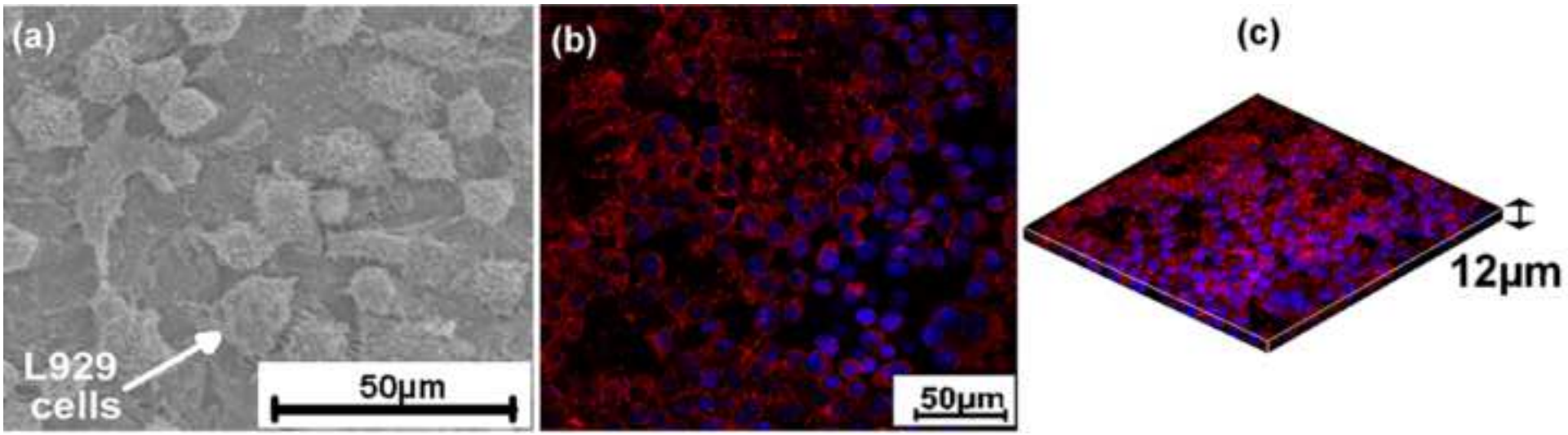

Figure 7 -Stained nuclei and F-actin patterns on the 88 Jmm3

Click here to download Figure FIEE67~1.TIF

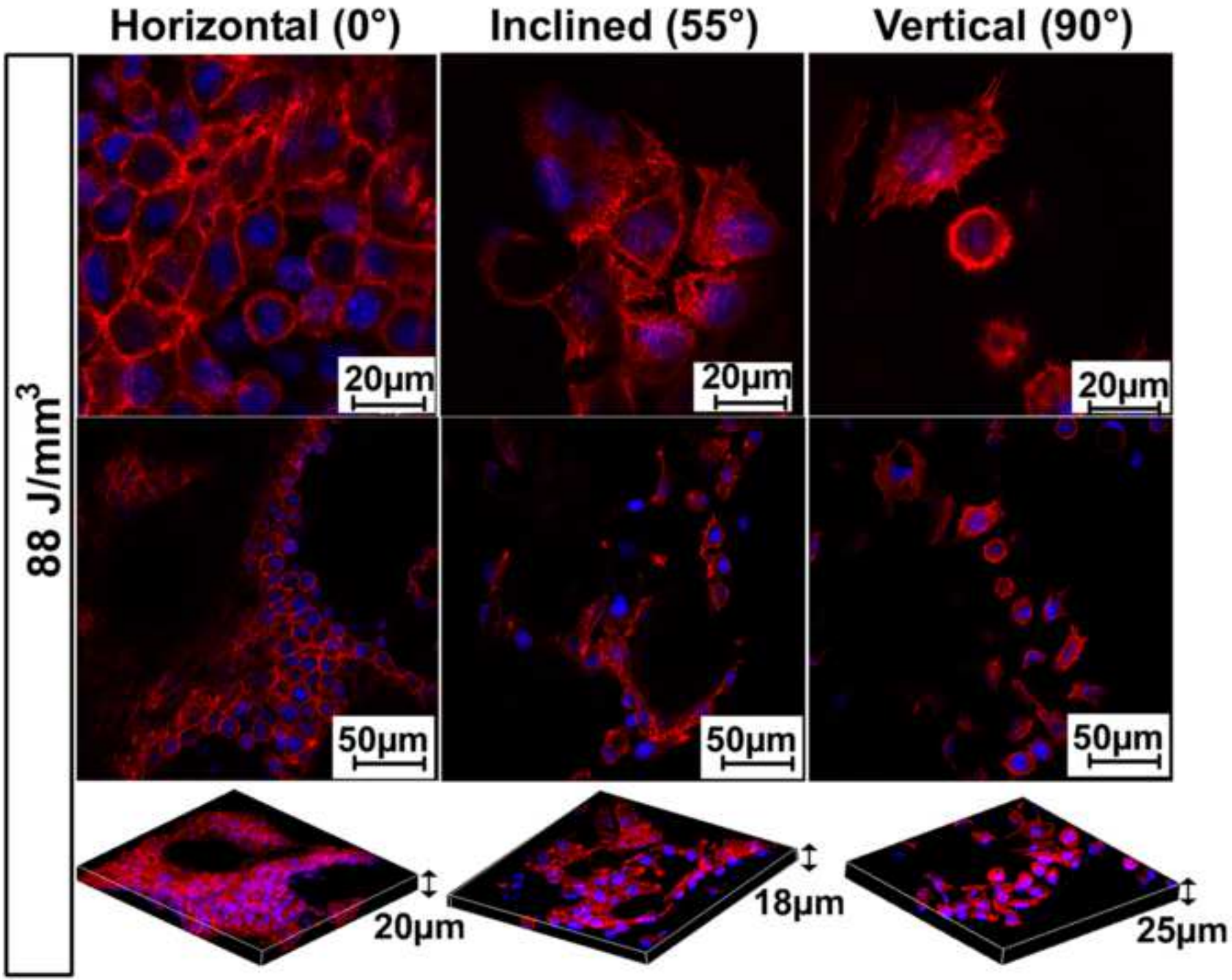

Figure 8 -Stained nuclei and F-actin on the 208 Jmm3

Click here to download Figure Figure 8 -Stained nuclei and F-actin on the 208 Jmm3.tif

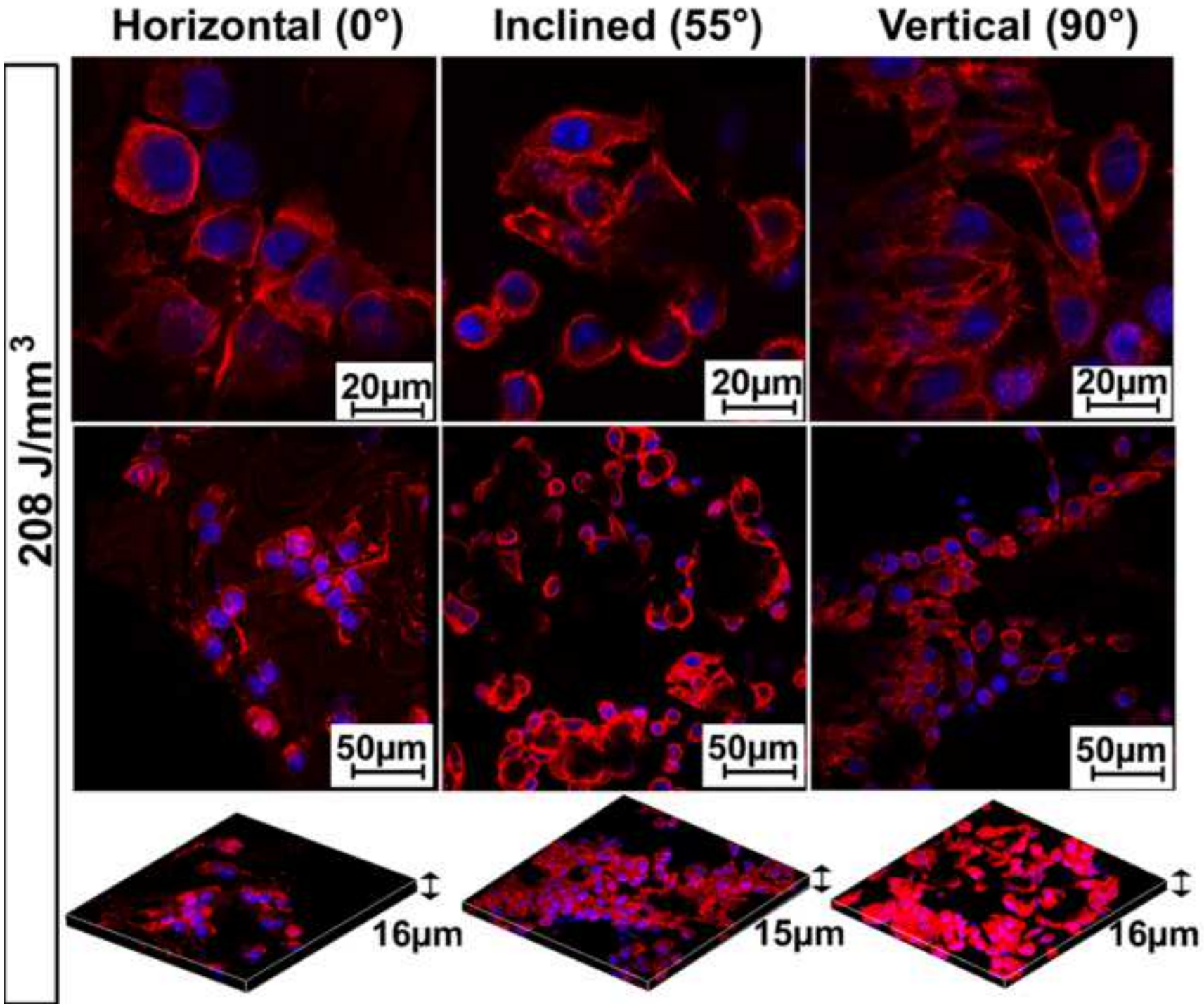

Figure 9 -Cell viability on the different build orientation

Click here to download Figure FIC864~1.TIF

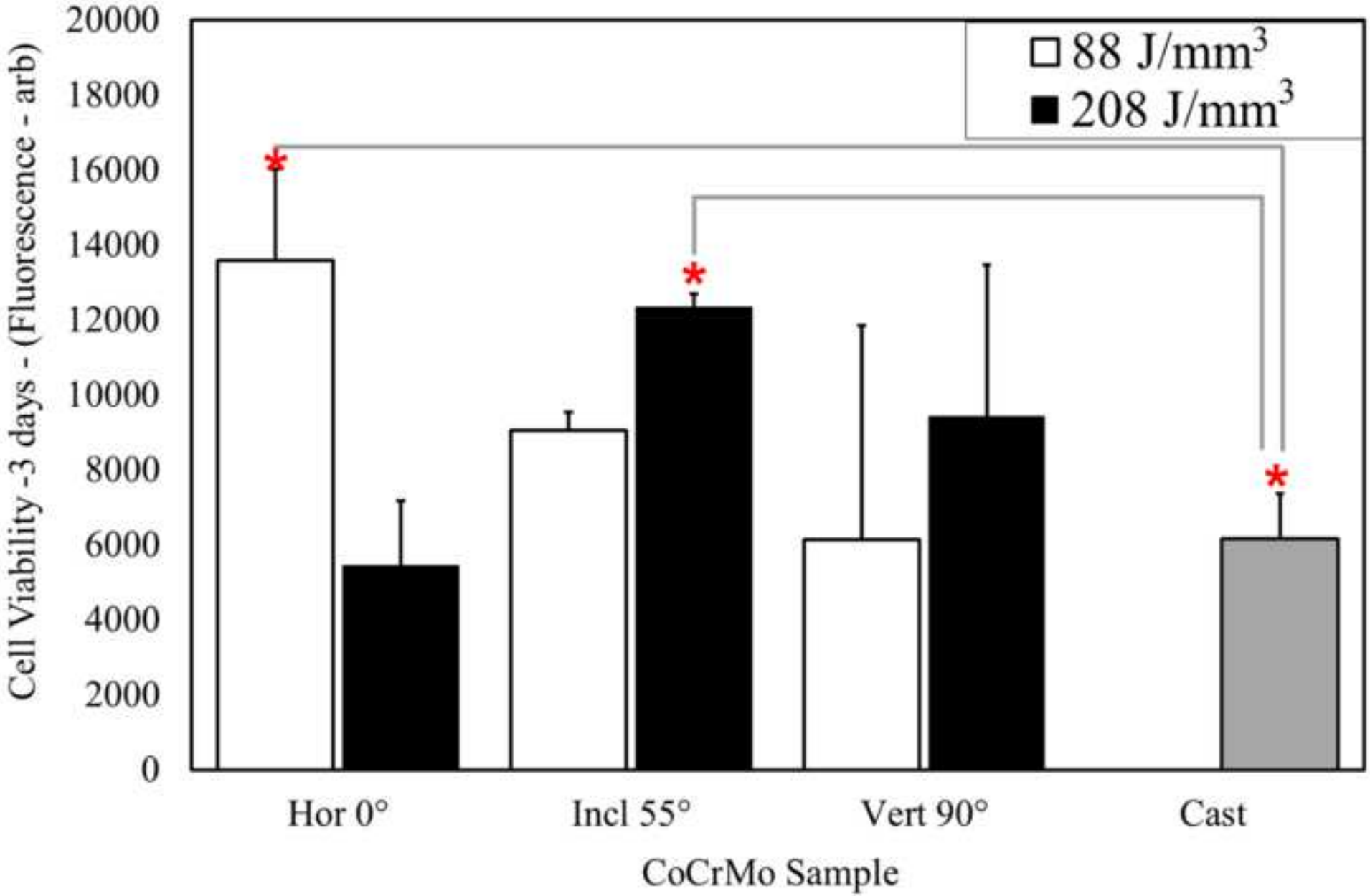

Figure 10 - Cytotoxicity of SLM CoCrMo

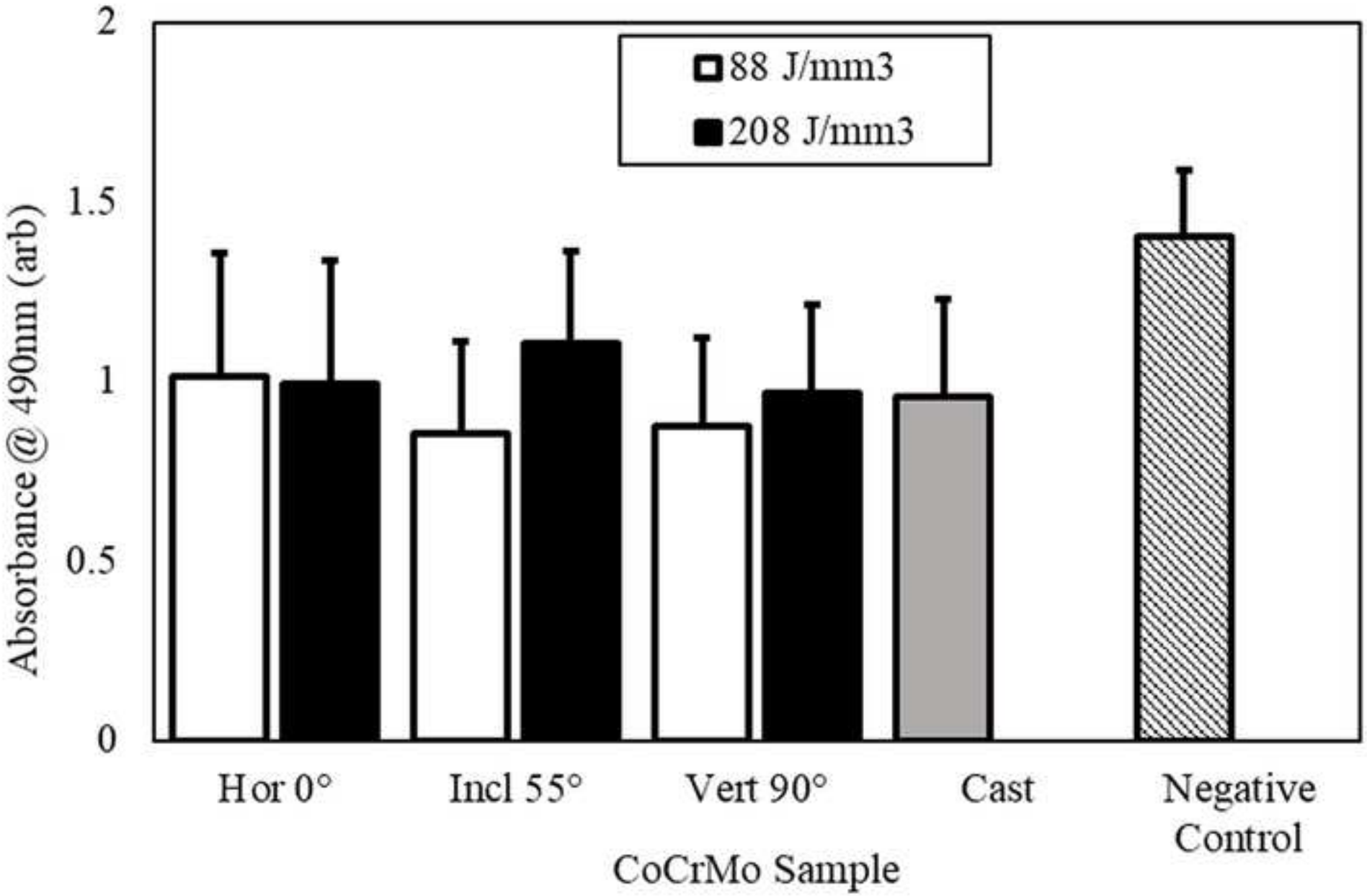

Figure 11 - Relevance of surface-Fuorescence

Click here to download Figure Figure 11-Relevance of surface-Fluorescence.tif

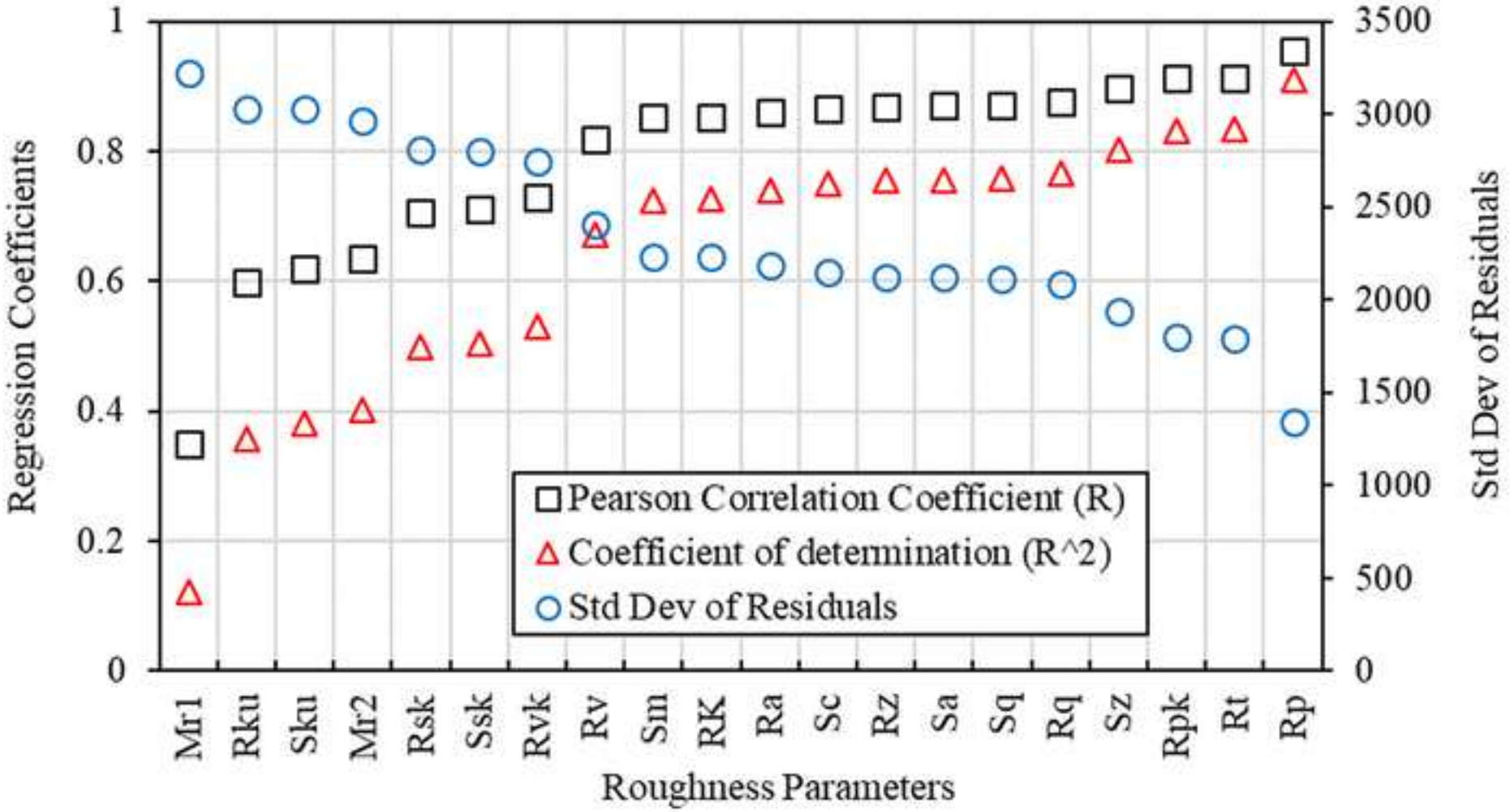

Figure 12 - Relevance of surface-absorbance

Click here to download Figure Figure 12-Relevance of surface-absorbance.tif

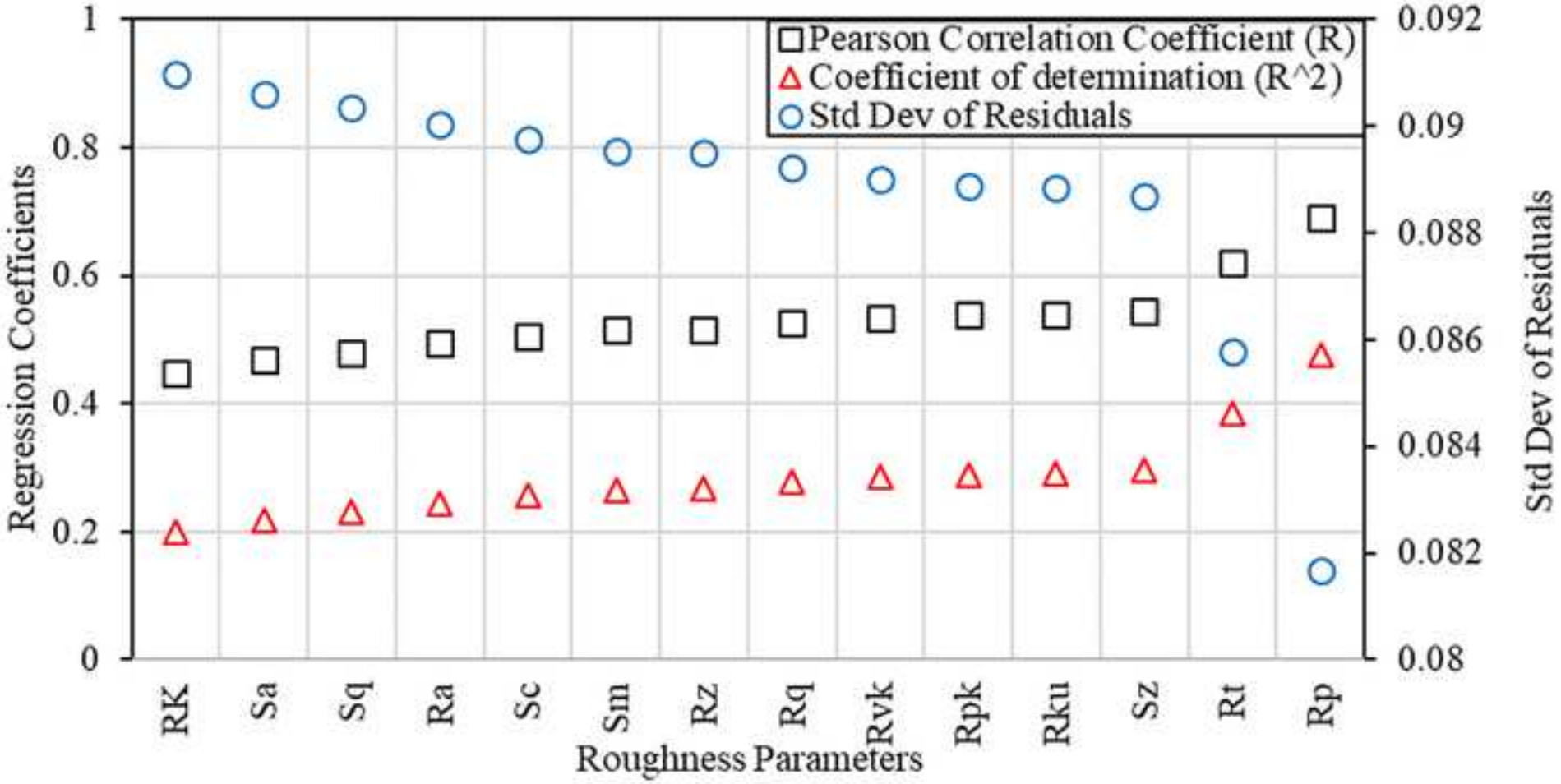

	Parameter	Meaning	Ref
(A)	Ra (µm)	Average roughness	[38]
	Rq (µm)	Root mean square parameter average roughness	[38]
	Rp (µm)	The height of the highest peak in the roughness profile	[38]
	Rv (µm)	Maximum profile valley depth	[38]
	Rt (µm)	Amplitude range. The sum of R_p and R_v.	[38]
	Rz (µm)	Mean maximal amplitude of five highest peaks	[39]
	Rsk	Skewness of amplitude distribution function (ADF).	[39]
	Rku	Kurtosis - the spikiness of the profile	[39]
(B)	Mr1 (%)	The fraction of the surface which consists of small peaks	[40]
	Mr2(%)	The fraction of the surface that consists of deeper valleys	[40]
	Rvk(µm)	Reduced valley depths along (x,y) from bearing ratio curve	[39]
	Rpk (µm)	Reduced peak height along (x,y) from bearing ratio curve	[39]
	Rk(µm)	Peak to valley roughness along (x,y) from bearing ratio curve	[39]
(C)	Sa (µm)	Average roughness within a definition area (A)	[41]
	Sq (µm)	Root mean square roughness within a definition area (A)	[41]
	Sz (µm)	The peak to valley height within area (A)	[41]
	Ssk	Skewness of the 3-D surface texture	[41]
	Sku	Kurtosis of the 3-D surface texture	[41]
(D)	Sm (mm^3/mm^2)	The mean spacing between peaks	[42]
	Sc (mm^3/mm^2)	Core void volume	[42]

Table 1: Definitions of the surface roughness parameters that were analysed for correlation with cell growth. The classification of the parameters is as follows: (A) 2D amplitude, (B) 2D functional, (C) 3D amplitude and (D) 3D functional. [38,39,41,42].

Surface Parameter (µm)	Ra	Std Dev	Rq	Std Dev	Rp	Std Dev	Rv	Std Dev	Rt	Std Dev
CoCrMo88 – (0°)	29.25	11.35	38.95	14.97	101.54	49.99	-72.67	28.95	174.22	67.26
CoCrMo 88- (55°)	25.51	7.35	31.01	7.63	67.05	17.40	-71.66	6.31	138.72	22.65
CoCrMo 88 - (90°)	7.43	0.55	9.22	0.65	27.23	4.26	-17.08	1.75	44.31	4.82
CoCrMo 208 - (0°)	14.74	2.76	18.16	3.16	41.38	9.71	-42.21	3.38	83.59	12.10
CoCrMo 208 - (55°)	20.62	2.68	25.97	3.18	76.14	11.10	-54.59	8.40	133.71	14.72
CoCrMo 208 - (90°)	12.11	0.66	14.90	0.79	45.82	1.76	-33.65	4.29	79.47	4.49
CoCrMo Cast	4.32	0.94	5.12	1.39	16.04	7.25	-10.39	1.02	26.44	7.43

Table 1: 2D amplitude surface characteristics of the SLM and cast Co-Cr-Mo discs characterised through interferometry.

.